JGR Earth Surface

RESEARCH ARTICLE
10.1029/2020JF005993

Quantifying Tectonic and Glacial Controls on Topography in the Patagonian Andes (46.5°S) From Integrated Thermochronometry and Thermo-Kinematic Modeling

Nevena Andrić-Tomašević[1,2], Sarah Falkowski[1], Viktoria Georgieva[3,4], Christoph Glotzbach[1], Manfred R. Strecker[4], and Todd A. Ehlers[1]

[1]Department of Geosciences, University of Tübingen, Tübingen, Germany, [2]Now at Institute of Applied Geosciences, Karlsruhe Institute of Technology, Karlsruhe, Germany, [3]Now at Institute for Earth Sciences/Institute of Physics and Mathematics, Universidad Austral de Chile, Valdivia, Chile, [4]Institute of Geosciences, University of Potsdam, Potsdam, Germany

Key Points:

- Low-temperature thermochronology records non-uniform erosion in the retro-wedge of the Southern Patagonian Andes
- Erosion pattern and long-wavelength topography are largely a function of regional tectonic activity over the last 15 Myr
- Glaciation has modified erosion rates and topography on sub-valley scales over the last 5–3 Myr

Supporting Information:

Supporting Information may be found in the online version of this article.

Correspondence to:

N. Andrić-Tomašević,
nevena.tomasevic@kit.edu

Citation:

Andrić-Tomašević, N., Falkowski, S., Georgieva, V., Glotzbach, C., Strecker, M. R., & Ehlers, T. A. (2021). Quantifying tectonic and glacial controls on topography in the Patagonian Andes (46.5°S) from integrated thermochronometry and thermo-kinematic modeling. *Journal of Geophysical Research: Earth Surface*, *126*, e2020JF005993. https://doi.org/10.1029/2020JF005993

Received 24 NOV 2020
Accepted 29 JUN 2021

Abstract The Patagonian Andes have been used to illustrate the dependency of major topographic changes in response to glacial erosion processes dominating over tectonic deformation and uplift. Here, we investigate tectonic and glacial contributors to the erosion history and evolution of topography in the Patagonian Andes at 46.5°S. We present 33 new apatite and zircon (U-Th)/He (AHe and ZHe, respectively) and fission track (AFT and ZFT, respectively) ages integrated with 46 previously published bedrock thermochronometric ages in a 3D thermo-kinematic model. Observed thermochronometer ages increase from the eastern flank of the topographic crest of the orogen toward the eastern retro-foreland basin (from AFT 4–10 Ma, ZHe 4–12 Ma, ZFT 6–14 Ma to AFT 28–32 Ma, ZHe 68–117 Ma). Thermo-kinematic modeling indicates that spatial gradients in thermochronometric ages can be explained by an up to 100-km-wide, parabolic-shaped pattern in exhumation rates with a maximum rate of 0.5 mm/yr from 15 Ma until the onset of glaciation at ~7 Ma. Furthermore, model results suggest that the youngest AHe ages require a localized acceleration in erosion from ~0.5 mm/yr to ~2.2 mm/yr starting between ~5 and ~3 Ma, coeval with intensified glaciation and subduction of the Chile Rise. Our results suggest that the long-wavelength (~100 km) topography and erosion patterns are likely controlled by rock uplift above mid-crustal ramp(s) and subsequent transpression along the Liquiñe-Ofqui Fault. Superposed on these tectonic processes, Late Cenozoic glaciation resulted in localized and accelerated erosion over wavelengths of <20 km.

1. Introduction

It has been known for a long time that topography reflects the interplay between the effects of tectonics, climate, biota, and surface processes (e.g., Champagnac et al., 2012; England & Molnar, 1990; Penck, 1953; Starke et al., 2020; Whipple, 2009; Whittaker, 2012). In orogens with multiple glaciations or a sustained, long-term glacial cover, glacial erosion is hypothesized to exert a major control on the development of topography (e.g., Egholm et al., 2009; Ehlers et al., 2015; Herman et al., 2013; Pedersen et al., 2010; Stock et al., 2009; Tomkin, 2007). It has been proposed that glacial erosion may balance rock uplift above the snowline and control mountain height independently from tectonically driven rock uplift rates (i.e., the "glacial buzz-saw" of Brozović et al., 1997). However, the glacial buzz-saw mechanism is restricted to regions dominated by warm-based glaciers that are characterized by high erosional efficiency (Brozović, et al., 1997). Cooler climate conditions at higher latitudes and/or higher elevations favor the development of cold-based glaciers characterized by decreased erosive capacity (Clinger et al., 2020; Thomson et al., 2010; Yanites & Ehlers, 2012). Under these circumstances, glaciers rather protect bedrock from erosion and preserve (high) topography (e.g., Pedersen et al., 2014; Tomkin & Braun, 2002).

Several previous studies have interpreted the exhumation patterns and topographic development of the Patagonian Andes (Figure 1) as dominantly controlled by climate (via glaciation) over the past 7 Myr (Herman & Brandon, 2015; Herman et al., 2013; Thomson et al., 2010). For example, low-temperature thermochronometric and modeling studies have suggested that latitudinal climate gradients are associated with variable glacial-erosion efficiency, such that warmer temperatures (and potentially warm-based glaciers)

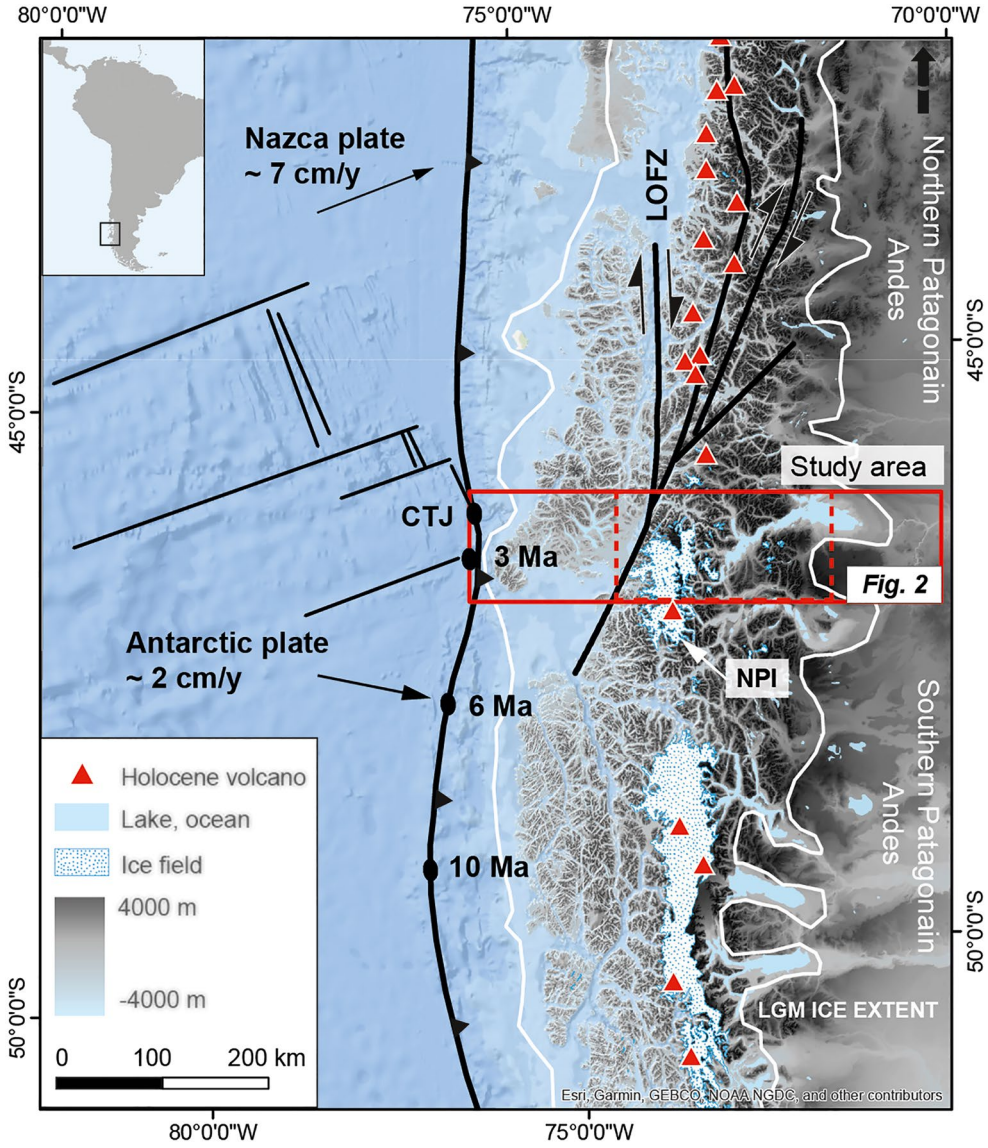

Figure 1. Topography and tectonic setting of the study area (dashed red rectangle). Red rectangle shows location of Figure 2. White line delineates glacial extent during the Last Glacial Maximum (LGM; Singer et al., 2004). Black ovals and ages show migration of the Chile Triple Junction (CTJ) in space and time since 10 Ma (Breitsprecher & Thorkelson, 2009). LOFZ-Liquiñe-Ofqui fault zone. Topography is illustrated by a 90 m-resolution DEM (GTOPO30 data). NPI–Northern Patagonian Ice field. The black arrows and velocities represent direction and rates of Antarctica and Nazca plates with respect to a fixed South American continent (e.g., Angermann et al., 1999; Wang et al., 2007).

are correlated with lower topography in the Northern Patagonian Andes and colder temperatures with higher topography in the Southern Patagonian Andes (Herman & Brandon, 2015; Thomson et al., 2010).

However, preceding and coeval with glacial conditions (starting between ~7 and ~5 Ma, Mercer & Sutter, 1982; Ton-That et al., 1999), this region had been affected by oblique plate convergence between the oceanic Nazca and the continental South American plate and collision of oceanic ridge segments on the Nazca plate, which have been accommodated by the regional Liquiñe-Ofqui strike-slip fault zone and associated structures (LOFZ, Figure 1; Astudilo-Sotomayor et al., 2021; Cande & Leslie, 1986; Forsythe & Nelson, 1985). Furthermore, an abrupt increase in present-day summit elevations (3,000–4,000 m), relief (regionally reaching almost 6,000 m considering fjord bathymetry) and a four-fold decrease in convergence rate (Figure 1, DeMets et al., 1990) can be observed south of the latitude of the Chile Triple Junction (CTJ; the intersection between the Nazca, Antarctic and South American plates at 46.5°S latitude), during the

last 6 Myr (e.g., Breitsprecher & Thorkelson, 2009). Other studies have suggested dynamic (transient) uplift associated with slab-window development (as a consequence of oceanic ridge collision) as an explanation for high topography in the Southern Patagonian Andes (Braun et al., 2013; Guillaume et al., 2009, 2013; Scalabrino et al., 2011). Finally, a crustal response to the closely spaced collision of ridge segments, manifested by local faulting, has been associated with observed abrupt short-wavelength topographic variations (Georgieva et al., 2016).

Most of the previous studies (Christeleit et al., 2017; Georgieva et al., 2016, 2019; Thomson et al., 2010) have focused on lower-temperature thermochronometers (^{4}He/^{3}He, apatite (U-Th)/He and fission track) that constrain the syn-glacial exhumation history of the Patagonian sector of the Andean orogen (last 7 Myr). However, distinguishing between climate versus tectonic influences on Patagonian topography, requires that the pre-glacial tectonic evolution of the Patagonian Andes needs to be considered. Therefore, in this study, we integrate new and published apatite and zircon (U-Th)/He (AHe and ZHe, respectively), as well as apatite and zircon fission track (AFT and ZFT, respectively) ages with a 3D thermo-kinematic numerical model. We aim at quantifying the tectonic and glacial contributions to exhumation, erosion and topography over the last 15 Myr, following the major mountain building phase. We determine the climatic (i.e., glacial) contributions to exhumation and topography by comparing the predicted ages from our numerical models with the observed AHe ages that are sensitive to thermal perturbations caused by glacial erosion and changes in topography (e.g., Densmore et al., 2007; Ehlers et al., 2006). Furthermore, combining lower (AHe) and higher temperature systems (AFT, ZHe, and ZFT) in our models allows us to record thermal perturbations in the upper crust (e.g., Reiners et al., 2003) that likely reflect pre- and syn-glacial tectonic contributions to exhumation (e.g., Michel et al., 2018; Rak et al., 2017).

2. Regional Setting

Here, we summarize the chronology of events relevant to the tectonic (kinematic) history of the Patagonian Andes that are needed for our thermo-kinematic model setup, which is used for the interpretation of thermochronometer data (briefly outlined in Section 2.3).

2.1. Regional Geologic Setting

The Patagonian Andes resulted from the subduction of the Nazca plate at the convergent South American plate margin over the last ~100 Myr (Figure 1; Folguera & Ramos, 2011; Fosdick et al., 2011; Ramos, 2009). Upper-plate shortening has been accommodated by several pulses of thick- and thin-skinned style thrust faulting concentrated in the retro-foreland (Fosdick et al., 2011; Ramos, 1989). Mountain building resulted in at least 25–40 km of shortening (at > 49°S latitude), and is associated with retro-foreland migration of deformation (Fosdick et al., 2011; Ramos, 1989). In the study area (Figure 2), the emplacement of the Jurassic to Cretaceous Patagonian Batholith in pre-Mesozoic basement preceded and partly occurred coevally with crustal shortening (Hervé et al., 1987; Hervé, Pankhurst, et al. 2007; Hervé, Faundez, et al., 2007).

Although the amount of upper-plate shortening was limited, the final and main mountain-building pulse in the Oligocene–Middle Miocene (~30–~15 Ma, Fosdick et al., 2011; Lagabrielle et al., 2004; Thomson et al., 2001) was associated with a significant exhumation of more than 6 km of rock (Fosdick et al., 2011, 2013; Thomson et al., 2001). Since the Oligocene, shortening has been accommodated by thrust faulting in the retrowedge (e.g., Folguera et al., 2018; Fosdick et al., 2011; Ramos, 1989). This tectonic phase is recorded by a transition from marine to continental deposition (molasse-type basin) in the retro-foreland occurring approximately synchronously along the entire Patagonian Andes (Fosdick et al., 2011; Ramos & Ghiglione, 2008).

Carbon and oxygen isotope analyses from paleosols in syntectonic deposits in the retro-foreland document the transition from humid to arid climate conditions at ~16–14 Ma (Blisniuk et al., 2005). This climate transition was controlled by the formation of the Andean orographic barrier due to uplift (Blisniuk et al., 2005). From ~15 Ma, sedimentation rates decreased in the eastern Basin Coeval with the termination of thrust activity (Blisniuk et al., 2005). Finally, at 12 Ma the formerly active deformation front in the eastern foreland was sealed by Miocene–Pliocene plateau basalts (e.g., Guivel et al., 2006), marking the minimum age for active orogenic growth at these latitudes.

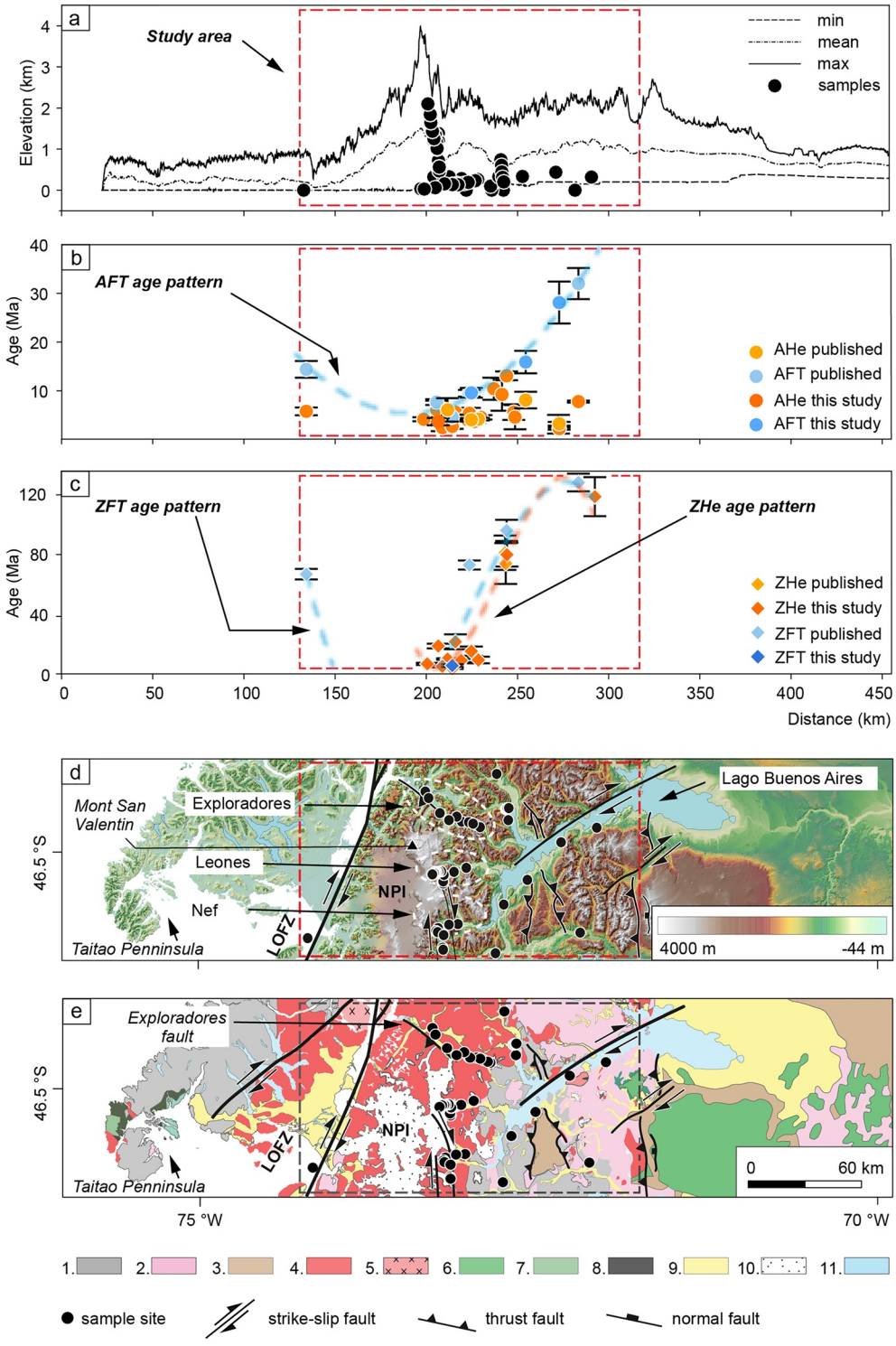

Figure 2.

The termination of Cenozoic shortening at 54°S was partially coeval with the onset of oblique oceanic-ridge collision starting at ~14 Ma (Breitsprecher & Thorkelson, 2009; Cande & Leslie, 1986). Successive ridge segments collided with the subduction margin at 14–12 Ma, 10 Ma, 6 Ma, 3 Ma, and 0.3 Ma, leading to the northward migration of the triple junction from the south (54°S) to its present position at 46°30′ S (Breitsprecher & Thorkelson, 2009; Cande & Leslie, 1986) and the northward unzipping of an asthenospheric slab window beneath southern Patagonia. This process is proposed to have been associated with a transient dynamic uplift of up to 0.7 km (Braun et al., 2013; Guillaume et al., 2009, 2013) and localized extension via reactivation of former thrust faults following the collapse of the uplifted and thermally weakened continental crust during the last 3–4 Myr (Lagabrielle et al., 2007; Scalabrino et al., 2010).

The location of the CTJ has remained relatively stable (47°50′–46°30′ S) over the last 3 Myr due to the closely spaced subsequent collisions of three short ridge segments, and it represents a major tectonic segmentation between the Northern and Southern Patagonian Andes. North of the CTJ, the Nazca plate subducts obliquely (N80°) at a rate of ~7 cm/yr (Figure 1; Angermann et al., 1999; DeMets et al., 1990). The margin-parallel component of oblique deformation is accommodated by the dextral transpressional intra-arc LOFZ (Rosenau et al., 2006). The LOFZ has been active since ~16–10 Ma and is associated with pronounced exhumation since ~7 Ma (Thomson, 2002). South of the CTJ, the subduction of the Antarctic plate beneath the South American continental plate is perpendicular at a rate of 2 cm/yr (Figure 1; Wang et al., 2007).

2.2. Geomorphology and Glacial History

The highest topography of the Patagonian Andes follows a N–S oriented axis (Figures 1 and 2d) and is intersected by numerous glaciated valleys separating the Northern Patagonian Icefield (NPI) from the eastern orogenic front (Lagabrielle et al., 2004; Scalabrino et al., 2010). The area to the east and south of the present CTJ is marked by a high topography (maximum elevation of 4,060 m, Mount San Valentín, Figure 2d) that decreases eastward toward the retro-foreland basin (Figures 1 and 2). The eastern orogenic front is characterized by a polycyclic, gently inclined and gravel-covered surface that merges with the low-relief topography of the Pampean region adjacent to the Atlantic Ocean (e.g., Clague et al., 2020). To the west of the highest topography of the Andes, the study area is flanked by the low-elevation corridor of the LOFZ that forms a steep boundary between the NPI and the Taitao Peninsula (Figure 2).

The study area has been repeatedly glaciated during the last 7–5 Myr (e.g., Lagabrielle et al., 2010; Mercer & Sutter, 1982; Singer et al., 2004), and numerous U-shaped valleys, overdeepenings, cirques, hanging valleys, and moraines demonstrate the strong glacial impact on the landscape. Moraines farther to the south (~49°S), however, may suggest an even earlier onset of glaciation at ~10 Ma (Wenzens, 2006). Compared to the present-day conditions the distribution of terminal moraines testifies to a significantly larger, regional ice extent with ice caps that reached widths of 100–300 km across the orogen (Figure 1, Clapperton, 1993; Singer et al., 2004). The present-day equilibrium-line altitude (ELA) in the NPI area is estimated to be between ~1,000 and 1,300 m (Rivera et al., 2007), while during the LGM it lowered to elevations between ~600 and 500 m (e.g., Broecker & Denton, 1989; Hubbard et al., 2005).

2.3. Thermochronological Data in the Study Area

The W–E distribution of AHe, AFT and ZFT data at elevations <500 m across the orogen shows a clear eastward increase of thermochronometric ages and an incipient U-shaped pattern (Figure 2; Georgieva

Figure 2. Distribution of new and published thermochronometric ages used in this study (Georgieva et al., 2016, 2019; Guillaume et al., 2013; Thomson et al., 2001, 2010). Red dashed rectangle represents the modeled study area. (a) Swath profile of the area inboard of the Chile Triple Junction with locations of samples used in this study (new and published); (b) Age versus distance distribution of new and published AHe and apatite fission track (AFT) ages (1 sigma error) from elevations <500 m. Dashed blue line represents AFT age pattern; (c) Age versus distance distribution of new and published ZHe and ZFT ages (1 sigma error) from elevations <500 m. Dashed blue and orange lines represent zircon fission track (ZFT) and ZHe age patterns; (d) Map showing topography, major structures, and thermochronologic sample locations. Dashed ellipses delineate Leones, Nef and Exploradores valleys. Topography is illustrated by a 90-m resolution DEM (GTOPO30 data); (e) Simplified geological map based on SERNAGEOMIN (2003). 1. Pre-Mesozoic basement, 2. Jurassic–Cretaceous volcanic and volcano-sedimentary rocks, 3. Cretaceous–Tertiary retro-foreland basin fill, 4. Cretaceous–Oligocene batholith, 5. Miocene batholith, 6. Eocene–Pliocene intraplate alkaline basalts, 7. Pliocene ophiolites, 8. Pliocene–Quaternary volcanic rocks, 9. Glacial sediments, 10. Ice sheet (Northern Patagonian Ice field [NPI]), 11. Glacial lakes.

et al., 2016, 2019; Guillaume et al, 2013; Thomson et al., 2010). Although the U-shaped age pattern shown in Figure 2 is defined by one data point west of the topographic divide, we consider this pattern representative as a similar U-shaped pattern is defined farther north with existing (more densely sampled) thermochronometric ages across the LOFZ and west of the divide (Thomson, 2002; Thomson et al., 2010). Such U-shaped pattern in the thermochronometric age distribution is also typical of thermochronometric ages in the fold-and-thrust belt to the south (at ~51°S, Fosdick et al., 2013).

The youngest ages are located in the eastern foothills of the NPI. The oldest ZFT ages are located in the vicinity of the eastern thrust front and correspond to the crystallization age of the Patagonian Batholith (~130–70 Ma; Hervé, Pankhurst, et al., 2007, Hervé, Faundez, et al., 2007, and references therein). Based on pluton-crystallization depths (calculated using Al-in-hornblende), previous studies have suggested an average exhumation rate of up to 0.2 mm/yr since the Cretaceous (Hervé et al., 1997; Thomson et al., 2001). In the central part of the orogen, AHe and AFT ages and $^{4}He/^{3}He$ cooling histories suggest average-exhumation rates of up to 0.5 mm/yr along the eastern foothills of the NPI, for the last ~10–12 Myr (Georgieva et al., 2016, 2019) and 0.25 mm/yr toward the southern slopes of the NPI (averaged over the last 7 Myr, Christeleit et al., 2017). Focusing mainly on AHe age patterns and $^{4}He/^{3}He$ thermochronometry, Christeleit et al. (2017) deduced rapid glacial incision and generation of most of the present-day relief in the NPI region since the beginning of glaciation sometime between 10 and 5 Ma. Based on thermal-history modeling of thermochronometric ages, Georgieva et al. (2016, 2019) proposed a stepwise exhumation history over the course of the last 10 Myr driven by glacial erosion and superimposed tectonic pulses related to oblique ridge-collision events.

3. Methods

Fifteen new granodioritic/granitic bedrock samples were collected along a ~100-km-long, approximately west–east oriented, horizontal transect that is, located to the north and east of the NPI along the Exploradores Valley (northern flank of the NPI), and along the southern shoreline of Lago Buenos Aires (Figure 2, see also Figures S1 and S2, Andrić-Tomašević et al., 2021, and Table 1). These samples were collected at the lowest possible elevation (between 28 and 741 m a.s.l.) to minimize the elevation dependence of thermochronometric ages.

The samples were analyzed with the AHe, AFT, and ZHe dating techniques, resulting in 22 new ages (Table 1). Furthermore, we analyzed 18 zircon mineral separates from previously collected samples (Georgieva et al., 2016) for ZHe (18 samples) and ZFT (2 samples) thermochronometry. Because previous ZFT ages from the Exploradores Valley are old and close to crystallization ages (Figure 2), we focused our new ZFT analyses on samples from the high-elevation area in the Leones Valley. To cover the possible range of ages, we selected a low- and a high-elevation sample for dating (327 and 2,100 m, Table 1). These samples originate from an elevation transect from the Leones glacier valley, which is an eastward-draining glacier of the NPI (Figure 2d). Finally, these new data were combined with 46 published AHe, 15 published AFT and 4 published ZFT bedrock thermochronometric ages from the region (Georgieva et al., 2016, 2019; Guillaume et al., 2013; Thomson et al., 2010; see also Table S1, Andrić-Tomašević et al., 2021). The samples were interpreted using a 3D thermo-kinematic numerical model. The combined data that are distributed along a horizontal transect (as close as possible at equal elevation) used to quantify the geometry of the exhumation field in the study region (Figure 2). In addition, some samples fall along the near-vertical Leones and Nef transects (see Section 4.2) to provide additional constraints on the rate and duration of exhumation. Note that among published samples we use only thermochronometric ages that can be interpreted as exhumation ages, that is, not as crystallization ages (Table S1, Andrić-Tomašević et al., 2021).

3.1. Low-Temperature Thermochronometry

Apatite and zircon separates of new bedrock samples were obtained by standard heavy liquid and magnetic mineral-separation techniques, and were then analyzed with AHe, AFT, ZHe, and ZFT dating methods at the University of Tübingen, Germany. A summary of sample locations and ages of this study is presented in Table 1. Details of individual sample measurements are provided in the supplementary material S1 (Tables S1–S7 available in Andrić-Tomašević et al., 2021).

Journal of Geophysical Research: Earth Surface
10.1029/2020JF005993

Table 1
Summary of New Thermochronological Ages

Sample	Longitude (°)	Latitude (°)	Elevation (m)	Lithology	AHe age (Ma)	AHe 1SD (Ma)	AFT age (Ma)	AFT 1SD (Ma)	ZHe age (Ma)	ZHe 1SD (Ma)	ZFT age (Ma)	ZFT 1SD (Ma)	Stratigraphic age (Ma)	
17PG005	−72.74387	−46.46489	741	Granodiorite	–	–	–	–	68.8	11.4	–	–	Cretaceous (Kig)	144–90 Ma
17PG006	−72.73897	−46.46521	605	Granodiorite	n.r.	–	–	–	71.3	5.5	–	–	Cretaceous (Kig)	144–90 Ma
17PG007	−72.73643	−46.46226	444	Granodiorite	n.r.	–	–	–	80.8	11.4	–	–	Cretaceous (Kig)	144–90 Ma
17PG008	−72.73121	−46.46079	313	Granodiorite	–	–	–	–	73.6	13.6	–	–	Cretaceous (Kig)	144–90 Ma
17PG009	−72.61126	−46.79708	335	diorite/ granodiorite	8.1	1.7	15.9	2.3	n.r.	–	–	–	Cretaceous (Kig)	144–90 Ma
17PG010	−72.36018	−46.62901	437	Granodiorite	3.2	0.4	28.1	4.3	–	–	–	–	Eocene (Eg?) or J3a	52–33 Ma
17PG011	−72.10095	−46.56931	320	Granite	–	–	–	–	118.0	13.0	–	–	Cretaceous to Tertiary (KTg)	
17PG013	−72.72285	−46.45991	203	Granodiorite	–	–	–	–	79.5	7.9	–	–	Cretaceous (Kig)	144–90 Ma
17PG015	−72.93237	−46.54082	231	Granodiorite	4.2	0.3	–	–	9.5	2.2	–	–	Cretaceous (Kig)	144–90 Ma
17PG016	−72.98170	−46.52432	190	Granodiorite	4.1	0.3	9.6	1.0	15.4	3.1	–	–	Cretaceous (Kig)	144–90 Ma
17PG017	−73.05421	−46.51865	133	Granodiorite	n.r.	–	–	–	9.2	1.1	–	–	Cretaceous (Kig)	144–90 Ma
17PG018	−73.09275	−46.48882	135	Granodiorite	–	–	–	–	21.6	5.0	–	–	Cretaceous (Kig)	144–90 Ma
17PG019	−73.14983	−46.50095	155	Granodiorite	6.1	2.4	–	–	10.1	0.5	–	–	Cretaceous (Kig)	144–90 Ma
17PG020	−73.21383	−46.46595	60	Granodiorite	3.7	0.8	–	–	18.8	1.5	–	–	Cretaceous (Kig)	144–90 Ma
17PG021	−73.28668	−46.39453	28	Granodiorite	–	–	–	–	6.9	0.7	–	–	Cretaceous (Kig)	144–90 Ma
VG11-LL-10	−73.1351	−46.7438	327	Granodiorite	–	–	–	–	3.9	0.3	5.8	0.9	Cretaceous (Kig)	144–90 Ma
VG12-CM-10	−73.2073	−46.7556	469	Granodiorite	–	–	–	–	5.3	0.6	–	–	Cretaceous (Kig)	144–90 Ma
VG11-LL-09	−73.2074	−46.7545	562	Granodiorite	–	–	–	–	5.3	0.5	–	–	Cretaceous (Kig)	144–90 Ma
VG12-CM-09	−73.2074	−46.7545	562	granodiorite		–	–	–	4.7	0.4	–	–	Cretaceous (Kig)	144–90 Ma
VG11-LL-05	−73.2158	−46.7842	722	granodiorite	–	–	–	–	8.1	0.6	–	–	Cretaceous (Kig)	144–90 Ma
VG11-LL-03	−73.2214	−46.7887	995	granodiorite	–	–	–	–	7.4	0.4	–	–	Cretaceous (Kig)	144–90 Ma
VG11-LL-08	−73.2221	−46.7392	1,005	granodiorite	–	–	–	–	6.0	0.5	–	–	Cretaceous (Kig)	144–90 Ma
VG12-CM-08	−73.2216	−46.739	1,016	granodiorite	–	–	–	–	8.4	1.3	–	–	Cretaceous (Kig)	144–90 Ma
VG11-LL-07	−73.2259	−46.7422	1,150	granodiorite	–	–	–	–	6.3	0.9	–	–	Cretaceous (Kig)	144–90 Ma
VG11-LL-04	−73.2163	−46.7934	1,197	granodiorite	–	–	–	–	7.7	0.3	–	–	Cretaceous (Kig)	144–90 Ma
VG12-CM-07	−73.2446	−46.7402	1,253	granodiorite	–	–	–	–	6.5	0.6	–	–	Cretaceous (Kig)	144–90 Ma
VG11-LL-06	−73.2357	−46.7416	1,351	granodiorite	–	–	–	–	6.7	1.0	–	–	Cretaceous (Kig)	144–90 Ma
VG12-CM-06	−73.2551	−46.7406	1,434	granodiorite	–	–	–	–	5.5	1.1	–	–	Cretaceous (Kig)	144–90 Ma
VG12-CM-05	−73.2666	−46.7379	1,645	granodiorite	–	–	–	–	9.0	0.6	–	–	Cretaceous (Kig)	144–90 Ma
VG12-CM-04	−73.2713	−46.7425	1,843	granodiorite	–	–	–	–	8.6	0.6	–	–	Cretaceous (Kig)	144–90 Ma
VG12-CM-03	−73.2887	−46.7469	2,100	granodiorite	–	–	–	–	11.7	1.8	14.4	1.8	Cretaceous (Kig)	144–90 Ma
VG12-CM-02	−73.3027	−46.7367	2,254	granodiorite	–	–	–	–	10.7	3.6	–	–	Cretaceous (Kig)	144–90 Ma
VG12-CM-01	−73.2959	−46.7349	2,436	granodiorite	–	–	–	–	12.2	1.3	–	–	Cretaceous (Kig)	144–90 Ma

Note. Stratigraphic ages after SERNAGEOMIN (2003). Full data sets are presented in the Tables S2–S7 (available in Andrić-Tomašević et al., 2021). n.r.–Single–Grain Ages Not reproducing.

3.1.1. Apatite and Zircon (U-Th)/He Dating

For each sample four apatite and four zircon grains were prepared for He, U, Th (and Sm for apatites) measurements, except for two samples (17PG006, 17PG007), where only two apatite grains of sufficient quality were available for measurement. Clear, euhedral grains, with diameters ≥80 μm, without fractures, and no or only small/few inclusions were selected, photographed, and packed into Nb capsules for analysis. Procedures of He measurements, mineral digestion, and analyses by ID-ICP-MS in the Tübingen laboratories are outlined in the supplementary material of Stübner et al. (2016). The α-ejection correction was done using the numerical approach by Glotzbach et al. (2019), which was also used to derive the grains' volumes, sphere-equivalent radii (ser), and effective uranium (eU) estimates (Tables S2 and S5). Single-grain ages were calculated with the non-iterative solution from Meesters and Dunai (2005).

3.1.2. Apatite and Zircon Fission-Track Dating

Fission track dating of apatite and zircon was performed using the external detector and ζ-calibration techniques (Hurford, 1990). Apatites and zircons were mounted in epoxy resin and Teflon, respectively, ground, and polished. The mounts were etched (apatites for 20 s in 5.5 M HNO_3 at 21°C, and zircons in a KOH:NaOH eutectic melt at 228°C for variable time lengths (35–65 h) depending on the grains' radiation damage (e.g., Donelick, 2005; Garver, 2003; Hurford, 1990), covered with mica detectors, and packed with age standards (Durango and Fish Canyon Tuff) and uranium-doped glasses (IRMM540, IRMM541) as flux monitors for irradiation at the FRM-II nuclear reactor in Garching, Germany. Micas were then etched in ~40%-HF for 30 min. Fission tracks and Dpar were counted/measured at 1,000X| × magnification with a Zeiss AxioImager microscope equipped with AutoScan stage system and software (Tables S3, S4, S6 and S7, available in Andrić-Tomašević et al., 2021).

3.2. Numerical Modeling

The numerical modeling was conducted by using a modified version of the 3D finite element thermo-kinematic model Pecube-D presented in McQuarrie and Ehlers (2015) and Whipp et al. (2009). The Pecube-D version of Pecube was modified from the original version (Braun, 2002a, 2002b, 2003) to account for detrital thermochronometer age prediction (not used in this study) and temporally and spatially variable kinematic fields in convergent orogens (used in this study). The model solves the 3D transient heat-transport equation by taking into account heat conduction from the fixed basal temperature boundary, heat advection resulting from tectonic activity and surface denudation, and radiogenic heat production within the continental crust. The model comprises three components including a: (a) thermal model; (b) kinematic model; and (c) an age-prediction model, all described below.

3.2.1. Thermal Model

We assume that the background heat flow is controlled by a conductive and advective heat transfer, and radiogenic heat production (e.g., Braun, 2002a). The effects of groundwater flow, hydrothermal fluid flow, and conductive heat flow produced by point sources (i.e., plutons) are not taken into account as no data documenting fluid flow is available from the region. The temperature field and heat transfer is described by the 3D advection-diffusion equation (Carslaw & Jaeger, 1959):

$$\rho c\left(\frac{\partial T}{\partial t}+v\frac{\partial T}{\partial z}\right)=\frac{\partial}{\partial x}k\frac{\partial T}{\partial x}+\frac{\partial}{\partial y}k\frac{\partial T}{\partial y}+\frac{\partial}{\partial z}k\frac{\partial T}{\partial z}+\rho A \quad (1)$$

where x, y, z are spatial coordinates, t is time, and T (x, y, z, t) is temperature. A, c, ρ, k, and v are crustal volumetric radiogenic heat production ($\mu W/m^3$), specific heat capacity (J/kg × K), rock density (kg/m^3), thermal conductivity (W/m × K) and vertical velocity (mm/yr) of rocks from the kinematic model, respectively. The main outputs of this model are transient time-temperature paths that are generated by tracking surface particles through the model domain.

3.2.2. Modeling Strategy, Assumptions and Limitations

The philosophy behind our modeling strategy was to test a sufficiently wide range of parameters that is, constrained by independent geological observations. Given this, we reduced the number of free parameters and avoided geologically implausible solutions. The model parameters and their ranges are summarized in Table 2.

Table 2
Thermal, Material and Kinematic Parameters Used in the Model Simulations

Property/Parameter	Model input value
Material properties	
Crustal thickness	35 km[a,b]
Thermal conductivity	2.5 W/mK[a]
Specific heat capacity	800 J/kgK[c]
Crustal density	2,700 kg/m^3[a]
Mantle density	3,200 kg/m^3[a]
Basal temperature	400–1,000°C
Surface temperature	10°C
Atmospheric lapse rate	5°C/km
Crustal volumetric radiogenic heat production	1 μW/m^3[d]
e-folding depth of crustal radiogenic heat production	10 km[d]
Mantle volumetric heat production	0.02 μW/m^3[a]
Kinematic parameters	
Maximum uplift rate	0.1–2.2 mm/yr
1/2 width of parabola	40:20:160 km
Location of the maximum uplift rate	55:5:80 km

[a]Turcotte and Schubert (2002). [b]van der Meijde et al. (2013). [c]Haenel et al. (1988), Touloukian et al. (1989) [d]Hasterok and Chapman (2011).

As in several previous studies (e.g., Glotzbach et al., 2011; Herman et al., 2010; Michel et al., 2018; Valla et al., 2010), in our simulations the thermal, kinematic and geometric parameters that we consider known (as defined in the literature), or that have little influence on model prediction, were kept constant. For example, thermal conductivity, crustal volumetric heat production, and specific heat capacity are spatially uniform and represented by standard values reported for granodiorite lithology and continental crust (Ehlers, 2005; Haenel et al., 1988; Touloukian et al., 1989; Turcotte & Schubert, 2002). We broke down the modeling procedure into a series of tests to investigate the first-order influence of free parameters (exhumation rates and timing, basal temperature and geometry of the exhumation field) on the predicted thermochronometric ages. A stepwise increase in model-experiment complexity is used to narrow down the controlling first-order effects of the tested parameters on predicted thermochronometric ages. Such an approach not only helps to avoid geologically implausible combinations of parameters, but also decreases computational time and storage required for these simulations (e.g., one simulation takes up to 250 h to run and requires ~20 GB temporary disc storage). Given the long simulation time associated with these experiments a 3D inverse modeling approach (e.g., genetic algorithm or smart search) is not feasible. However, we note that our choice of investigating a range of parameters is akin to the Monte Carlo modeling approach, with the difference being that our stepwise increase in model complexity and decades of previous experience with thermal modeling problems similar to this allows us to narrow down the plausible range of parameters worth considering.

Our model domain represents a 200 × 100 km wide and a 35-km-thick block of continental crust, which corresponds to the average Moho depth in the Southern Patagonian Andes (e.g., van der Meijde et al., 2013). The horizontal resolution of the model is 0.5 km. The vertical model resolution varies from a 1:1 aspect ratio down to the first 5 km below the surface, 3:1 from 5 to 15 km depth, and 9:1 from 15 km depth. By default, the lower boundary is set by a basal temperature of 700°C (Tesauro et al., 2013) that is, kept constant during model evolution (Figure 3a). Pecube uses a fixed basal temperature as a boundary condition and does not allow free temporal variation of temperature (Braun, 2002a, 2002b, 2003). Normally, for the application of a constant temperature-boundary condition it is preferred to apply the boundary condition at the lithosphere-asthenosphere thermal boundary layers (e.g., ~110 km depth; S. D. Willett et al., 2020). However, due to the presence of a slab window in this location and previous, independently derived Moho estimates of temperatures at a shallower depth (Tesauro et al., 2013), we applied the best estimate available in the literature. Furthermore, we evaluated the sensitivity of results to our assumed basal temperature in Figure S5. An implication of this assumption is that the fixed temperature at the base of the crust suppresses the thermal gradient leading to different estimates of exhumation rates than in inversion models with fixed flux boundary conditions (S. D. Willett et al., 2020). However, this difference in model behavior is reported for processes involving high erosion rates over timescales greater than 10 Myr, which is not the case in our study. Furthermore, the average erosion rates that are predicted for the Late Miocene by our models and inverse thermal history models used by Georgieva et al. (2019) show no differences.

A surface temperature of 10°C was used as an upper thermal boundary at sea level with a lapse rate of 5°C/km. These values represent mean values of the surface temperature at sea level and lapse rate in the study area over a time span of 30 years (Worldclim data set, Fick & Hijmans, 2017). On the margins of the model domain, zero-flux boundary conditions were used. Although numerous geomorphologic indicators show that glaciation significantly affected topography in the study area, in our modeling approach we use present-day conditions (90 m resolution DEM, STRM) as the initial topography. In this way, we avoided the usage of unconstrained parameters representing pre-glacial topography and additional model complexity. Furthermore, in our simulations, topography remained constant during simulations assuming a topographic steady-state, that is, erosion rate equals tectonic rock-uplift rate during each time step.

To quantify the AHe thermochronometric age response to changing topography we used the approach of Olen et al. (2012) to iteratively solve (i.e., invert) for paleotopography until the misfit between observed and predicted thermochronometric age was sufficiently minimized (see details in Olen et al., 2012). We tested the effect of topographic variations on AHe ages during the last 7 Myr that corresponds to the onset of glaciation.

3.2.3. Kinematic Model

The kinematic model is based on two possible uplift fields in the study area. These fields include a uniform vertical and a parabola-shaped (laterally variable) vertical uplift (Figure 3b). The parabolic uplift field is based on Fermi's equation and parameterized by maximum and minimum uplift rates, as well as the width

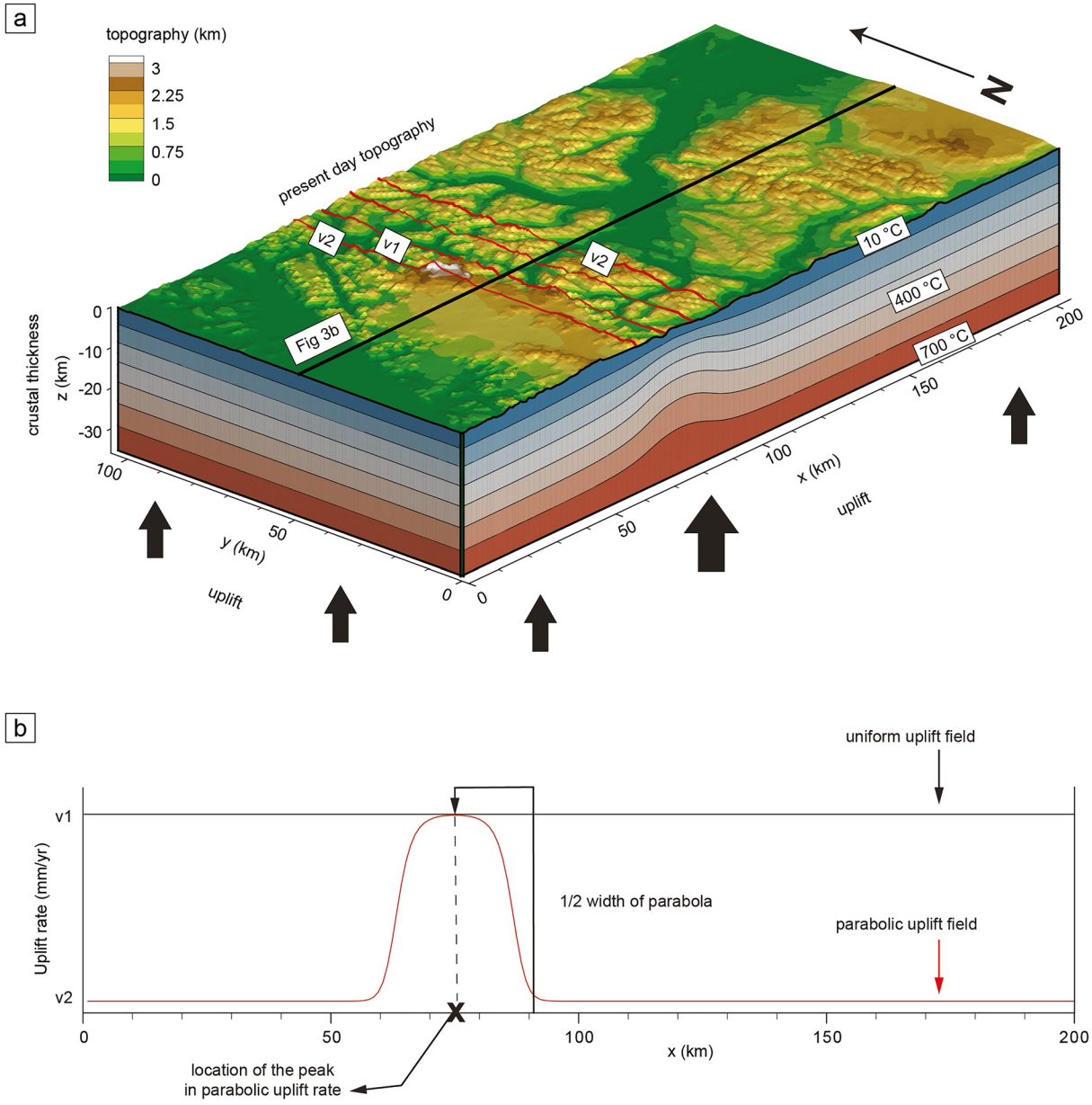

Figure 3. Model setup and kinematic field. (a) Model domain and boundary conditions; this case represents a parabolic uplift field (thick black arrows; red solid lines mark isolines representing the distribution of the uplift velocities); (b) kinematic fields simulated in this study: uniform uplift (black) and parabolic uplift (red).

and location of the parabola (Figure 3b). For the sake of simplicity, a cylindrical uplift pattern is adopted in all parabolic uplift models to extend the parabola into the third (North–South) dimension. The spatially uniform uplift pattern was used to test for a potential effect of a slab window-induced, long-wavelength uplift on the distribution of the predicted thermochronometric ages and to simulate average exhumation rates controlled by glacial erosion. The parabolic uplift pattern simulates: (a) antiformal stacking associated with ramp-flat thrust geometries as observed in numerous fold-and-thrust belts (e.g., McQuarrie & Ehlers, 2017), and (b) restraining bend kinematics as seen in many transpressional systems (e.g., Cunningham, 2007; Wakabayashi et al., 2004) potentially associated with the activity of the LOFZ. The purely vertical parabolic uplift pattern is an acceptable assumption to simulate thrust-related antiformal stacking in the study area for two reasons. First, previous studies in the Patagonian Andes found a low magnitude of shortening and higher vertical than horizontal velocity components in the retro-foreland resulting from the material transport along the steeply dipping thrust ramps (e.g., Fosdick et al., 2011, 2013; cf. Section 2.1). Second, the lack of field kinematic data on thrust activity in the studied region hinders an evaluation of the horizontal thrust component affecting predicted thermochronometric ages. The uncertainties in the horizontal thrust component would add poorly constrained complexity to the model. Finally, our consideration of a uniform vertical exhumation field is admittedly pedagogic and aimed at understanding if the simplest approach possible satisfies observations. Furthermore, it allows identification of the range of exhumation rates required to fit ages, thereby guiding what range of rates should be considered in complicated (parabolic) kinematic models.

3.2.4. Age-Prediction Model

The predicted thermochronometric ages across the surface topography are calculated from time–temperature paths using cooling rate dependent kinetic models. AHe and ZHe ages are predicted using diffusion kinetics from Farley (2000) and Reiners et al. (2004), respectively. AFT and ZFT ages are predicted using the annealing models of Green et al. (1986) and Galbraith and Laslett (1988), respectively.

3.3. Evaluation of Modeling Results

We conducted 495 simulations divided into 7 experiments (Table S8). Each simulation is evaluated by the goodness of fit between predicted and observed thermochronometric ages, defined by a reduced χ^2 misfit.

The quality of fit between predicted and observed thermochronometric ages in each simulation for each individual thermochronometer system was calculated as (e.g., Dunai, 2005; Ehlers et al., 2003):

$$\chi 2 = \sqrt{\frac{1}{n} * \sum_{i=1}^{n} \frac{\left(\text{Pred.}_i - \text{Obs.}_i\right)^2}{\text{Error}^2}} \tag{2}$$

where n is the number of samples, Pred. is the predicted thermochronometric age, Obs. is the observed thermochronometric age and Error is the 1 σ uncertainty of the observed age. A χ^2 misfit that equals 2 represents a fit within 2 standard deviations. Higher values indicate a progressively worse fit, for example, χ^2 misfit of 5 represents a fit within 5 standard deviations.

The cumulative χ^2 misfit for all samples and thermochronometers in each simulation was calculated as:

$$\chi^2_{\text{Cum}} = \chi^2_{\text{AHe}} + \chi^2_{\text{AFT}} + \chi^2_{\text{ZHe}} + \chi^2_{\text{ZFT}} \tag{3}$$

We consider a model appropriate when the χ^2 misfit for each thermochronometer is below or equal to 2 (fit within 2σ of sample uncertainties). In the case of the cumulative χ^2 misfit, we consider a model to be adequate at values of 8 and lower. The best-fit scenario from each experiment was generally used as a reference model in the subsequent experiment. Deviations from this approach are specifically mentioned and explained in the text.

4. Results: Observed Thermochronometric Ages

The new AHe and ZHe ages range from 3.7 ± 0.8 Ma to 8.1 ± 1.7 Ma, and 3.9 ± 0.3 Ma to 118.0 ± 13.0 Ma, respectively (±1σ, Table 1). The AFT and ZFT ages range from 9.6 ± 1.0 Ma to 28.1 ± 4.3 Ma, and 5.8 ± 0.9 Ma to 14.4 ± 1.8 Ma, respectively (±1σ, Table 1). All new AHe, AFT, and ZFT ages are from igneous rocks and are younger than the crystallization age (~130–70 Ma Patagonian Batholith; Hervé, Pankhurst, et al., 2007, 2007b, and references therein), whereas ZHe ages from samples 17PG005–008, 17PG011, and 17PG013 correspond to the crystallization age of the batholith (Table 1). In general, thermochronometric ages similar to the crystallization ages are observed along the eastern orogenic front. In contrast, thermochronometric ages younger than the ~130–70 Ma batholith crystallization age (referred to as "reset ages") occur near the high topography of the range and along the northern and eastern flanks of the NPI (Figure 2). The "younger" reset thermochronometric ages can be divided into two groups. The first group includes thermochronometric ages older than 7 Ma (pre-glacial), for which we assume that they were not affected by a potential acceleration in glacial erosion and/or direct processes of ridge collision and slab window development (since ~3 Ma) in the study area. The thermochronometric ages range between ~8–14 Ma for AHe, ~8–32 Ma for AFT, ~8–20 Ma for ZHe, and ~15 Ma for the ZFT system (Tables 1 and S1, and Figures S1 and S2). These ages suggest that they were likely affected by previous tectonic events during the main mountain building phase of the region (~30–15 Ma, e.g., Fosdick et al., 2011; Lagabrielle et al., 2004) and activity of the LOFZ (since 16–10 Ma; Cembrano et al., 2002; Thomson, 2002). In contrast to the ZHe and ZFT ages that are only available from a narrow zone in the immediate foothills of the NPI (from the Exploradores, Leones and Nef valleys, Figures S1 and S2), AHe and AFT ages are available from along the eastern orogenic front. The second group of "younger" thermochronometric ages includes ages that are younger than 7 Ma. With the exception of several AHe ages obtained along the valley occupied by Lago Buenos Aires (Figures 2, S1 and S2), the samples for all other ages <7 Ma were located along the flank of the NPI.

The new thermochronometric ages are consistent with published data from the same thermochronometric systems (Georgieva et al., 2016, 2019; Guillaume et al., 2013; Thomson et al., 2010; see also Table S1).

4.1. Horizontal Transect Thermochronometric Ages

Along the horizontal E–W transect, thermochronometric ages range between 3.7 ± 0.8 and 6.1 ± 2.4 Ma for AHe, 9.6 ± 1.0 Ma and 28.0 ± 4.3 Ma for AFT, and between 6.9 ± 0.7 Ma and 118.0 ± 13.0 Ma for ZHe (±1σ, Table 1). In the Exploradores Valley (northern flank of the NPI, Figure 2d), most ZHe ages show variations at spatial scales of <10 km along the valley ranging from ~10 Ma to ~20 Ma (Figure S1). These spatial variations might be related to differential exhumation controlled by the Exploradores thrust fault (Georgieva et al., 2016).

New and published thermochronometric ages from elevations <500 m (to eliminate elevation effects on the thermochronometric ages, Figures 2b and 2c) along the W–E horizontal transect delineate in general a U-shaped age pattern, with young ages (AHe ~2–6 Ma, AFT ~4–9 Ma, ZHe ~4–21 Ma, and ZFT ~5.8 Ma, Table S1) at the foothills of the NPI in the west and older ages (AFT ~15–28 Ma, ZHe ~73–118 Ma, and ZFT ~72–127 Ma, Table S1) toward the retro-foreland in the east (Figures 2b and 2c). The spatial distribution of the AFT, ZHe, and ZFT ages show concave-upward (U-shaped) patterns with minima centered along the immediate eastern foothills of the NPI (Figures 2b and 2c). We note variations in the widths of the proposed U-shape age patterns between different thermochronometers. ZHe and ZFT U-shaped age patterns are narrower (~100 km wide, Figure 2c) compared to the AFT U-shaped age pattern (~150 km wide, Figure 2b) and show a steeper gradient in thermochronological ages as they approach the NPI from the east. The AHe thermochronological ages delineate a clear increase in age toward the east (Figure 2b).

Furthermore, the AHe and AFT ages from the immediate eastern foothills of the NPI define a concave-upward pattern in the N–S direction (at wavelengths of ~50 km, Figures 4b and 4c). Thermochronometric ages decrease from north to south from the Exploradores to the Leones Valley (~4 Ma to 2 Ma AHe ages, ~9.5 Ma to 4 Ma AFT ages, ~9 Ma to 4 Ma ZHe ages) and increase again from the Leones toward the Nef Valley (~2 Ma to 4 Ma AHe ages, ~4 Ma to 7 Ma AFT ages; Figure 2d). In both directions, W–E and N–S, the Leones Valley shows the youngest thermochronometric ages and thereby defines an area of localized rapid exhumation.

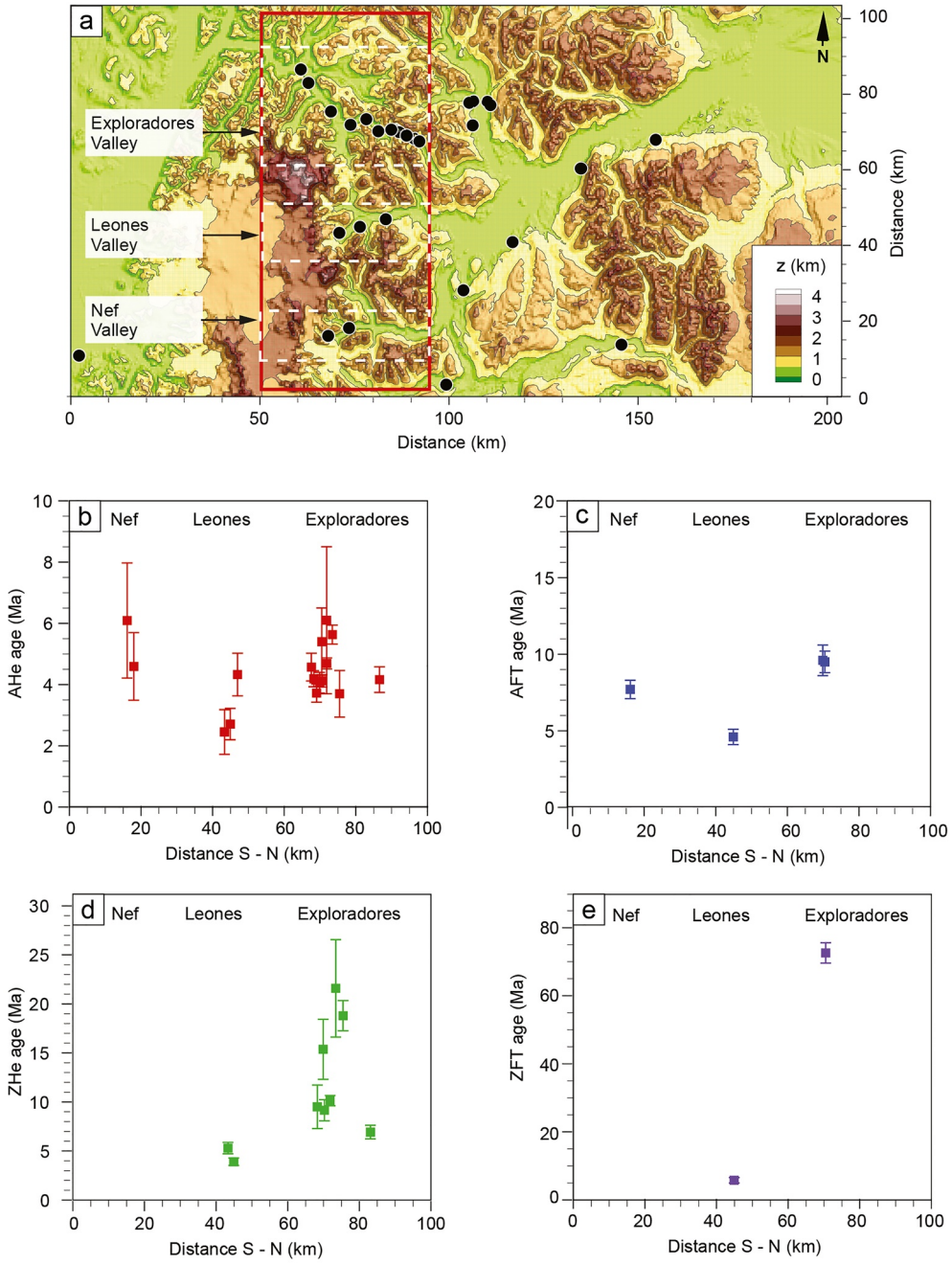

Figure 4. S–N distribution of thermochronometric ages along the northern and eastern foothills of the Northern Patagonian Icefield (NPI). (a) Sample locations (black dots; new and published) from elevations <500 m only to avoid elevation-effects on ages. Red rectangle delineates samples whose thermochronometric ages are plotted in b, c, d and e. (b, c, d, e) Spatial distribution of AHe (b), apatite fission track (AFT) (c), ZHe (d), and zircon fission track (ZFT) (e) thermochronometric ages in the N-S direction. The distance is measured from the center of the coordinate system of our model domain that is, located in the Golfo de Peñas (47°S, Figures 1 and 3).

4.2. Age-Elevation Transect

Previously reported AHe and AFT ages from an elevation transect in the Leones Valley (Figures 2, 4 and 5; Georgieva et al., 2016, 2019) range between 2.0 ± 0.6 Ma and 6.8 ± 1.1 Ma, and 4.6 ± 0.5 Ma and 7.7 ± 1.2 Ma, respectively. Here, we report 18 new ZHe and 2 new ZFT thermochronometric ages from the same samples. The transect covers an elevation range between 325 and 2,436 m (min/max elevations in the catchment

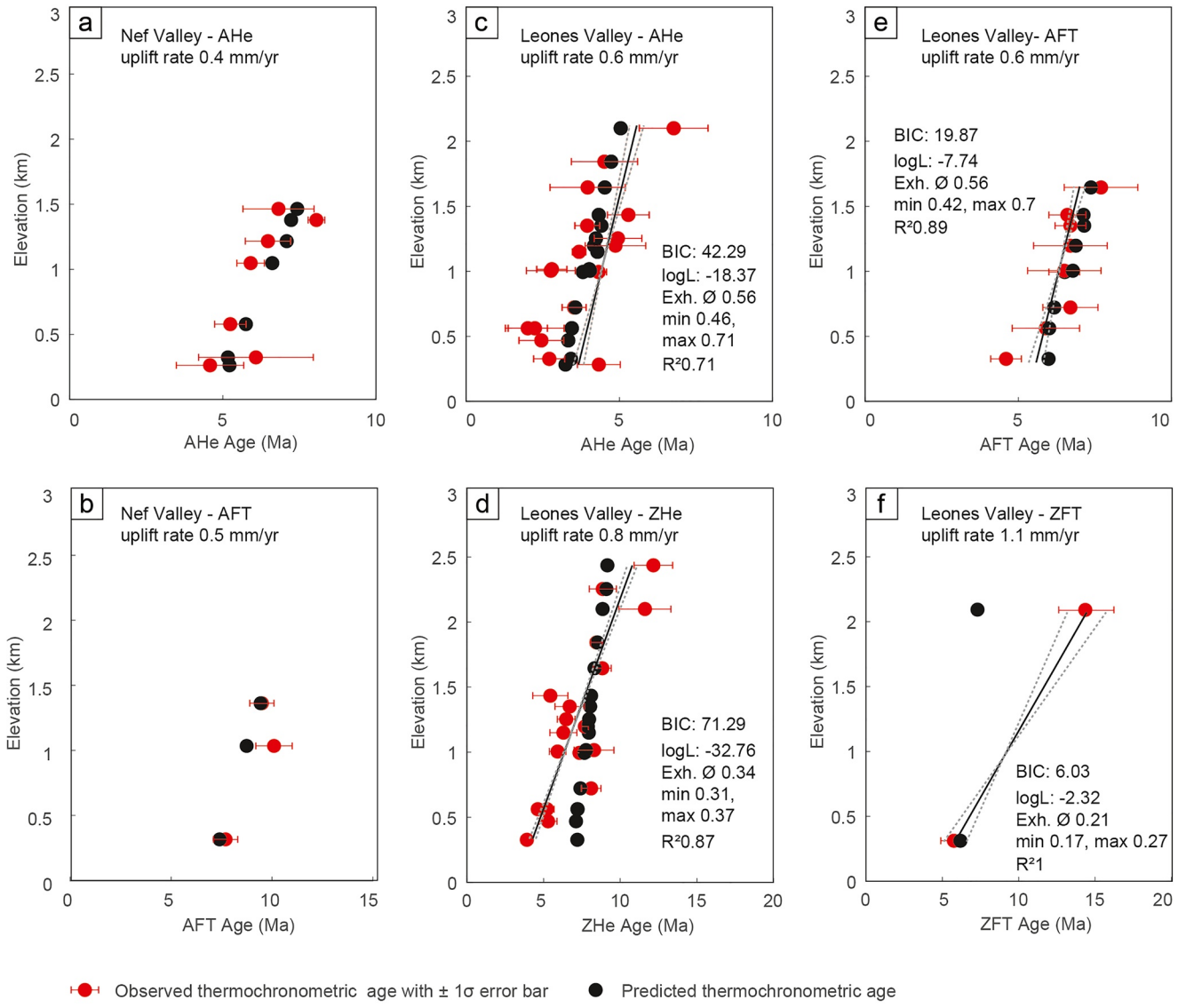

Figure 5. Age-elevation profiles in the Nef and Leones valleys (see Figure 4) comparing observed (ZHe and zircon fission track (ZFT) thermochronometric ages, red circles–this study; AHe and apatite fission track (AFT) thermochronometric ages–Georgieva et al., 2016, 2019) and predicted thermochronometric ages (black circles, this study). Predicted thermochronometric ages result from simulations exploring the effect of different uniform rock-uplift rates with a basal temperature of 700 °C. These simplified, uniform-uplift simulations were conducted to approximate rock-uplift rates to be further explored in subsequent simulations with more complex kinematics. Panels (a, b) predicted versus observed AHe and AFT thermochronometric ages in the Nef Valley; (c, d, e, f) predicted versus observed AHe, ZHe, AFT, and ZFT thermochronometric ages in the Leones Valley. The black and gray dashed lines represent a least squares fit of independent slopes to AHe, AFT and ZHe age-elevation relationships. For details on the slope calculation see Glotzbach et al. (2011). Variables shown in plots include: the Bayesian Information Criterion (BIC); log-likelihood (InL); average apparent exhumation rate (Exh. Ø); minimum/maximum apparent exhumation rate (min, max) within xy-uncertainty; and correlation coefficient R^2.

~230/3,750 m) with a corresponding range of ZHe and ZFT ages from 3.9 ± 0.3 Ma to 12.2 ± 1.3 Ma, and 5.8 ± 0.9 Ma to 14.4 ± 1.8 Ma, respectively (Table 1).

ZHe ages correlate positively with elevation (r^2 = 0.87, Figure 5d) with a slope of 0.34 ± 0.03 mm/yr implying lower apparent exhumation rates compared to those calculated from AHe (0.56 ± 0.125 mm/yr, r^2 = 0.71) and AFT data (0.56 ± 0.14 mm/yr, r^2 = 0.89, Figures 5c and 5e). It is notable that in the Leones Valley, AHe ages decrease with increasing altitude, from the lowest elevations of 283 m to elevations of ~993 m, Table S1, Figure 5c).

The ZFT ages also correlate positively with elevation, but given the limited number of data the slope range of 0.17–0.27 mm/yr is ambiguous (Figure 5f). The thermochronometric age difference between thermochronometer systems increases at higher elevations (e.g., ~7.5 Myr at 2,100 m a.s.l. vs. ~3 Myr at 327 m a.s.l. between AHe and ZFT thermochronometric ages, Table 1) suggesting significant compression of the isotherms below the lower part of the valley.

5. Numerical Modeling Results

5.1. Considerations of Experimental Design

Before presenting the experimental design for the numerical simulations, we discuss a series of potential complexities in the study area, and justify the simplifications that we have made in our experiments. The broad U-shaped distribution of observed thermochronometric ages across the study area (W–E, covering ~100–150 km, Figures 2b and 2c, see details in Section 4) suggests either: (a) differential exhumation due to tectonically induced rock uplift and associated erosion (e.g., McQuarrie & Ehlers, 2015); and/or (b) differential exhumation due to erosion of the pre-existing topography (e.g., Braun, 2005; Ehlers et al., 2006) in the last 15 Myr. These effects could be enhanced by lateral variations in the crustal temperature gradients caused either by shallow (i.e., plutons, Ehlers, 2005) or deeper (slab window) heat sources (e.g., Braun, 2010; Braun et al., 2013; Guillaume et al., 2013). In the following steps, an incremental increase in model complexity was used to identify the different components and sources of rock cooling observed in the data. We briefly summarize here the primary factors explored in subsequent simulations.

Although many observed that AHe ages correlate with the development of the slab window in the area (since ~4 Ma, Breitsprecher & Thorkelson, 2009), the observed width (wavelength) of the AHe U-shaped age pattern is too short to be controlled by the dynamic topography uplift driven by the thermal effects of the slab window (wavelength of ~250 km; Braun et al., 2013). Also, the associated uplift of less than 1 km suggested by previous studies (Braun et al., 2013; Guillaume et al., 2009, 2013) is not sufficient to reset AHe ages, which typically have closure-temperature depths of 2–3 km (Ehlers, 2005). Furthermore, during the last 3 Myr the study area was subjected to the collision of several ridges (e.g., Breitsprecher & Thorkelson, 2009). However, current thermochronological data show no evidence of a possible effect on upper crustal structures (Georgieva et al., 2016). Therefore, the immediate effect of ridge collision on shortening during the last 3 Myr is difficult to assess based on available observations. Finally, it is noteworthy, that the U-shaped age pattern previously described also applies to the higher-temperature thermochronometers ZHe and ZFT, which are usually not affected by the variations in pre-existing topography in contrast to AHe ages (e.g., Densmore et al., 2007; Ehlers & Farley, 2003). Therefore, erosion of the pre-existing topography alone cannot explain the spatial distribution of observed thermochronometric ages, especially in the case of the higher-temperature systems.

Lateral variations in the crustal temperature gradients as contributors to the wavelength of the observed U-shaped age patterns are also unlikely. The wavelengths (100–150 km in E–W direction and ~50 km in N–S direction, Figures 2 and 4) of the observed U-shaped age pattern could suggest the existence of a shallow heat source (pluton) within the crust. However, the consistent age-elevation relationship of thermochronometric ages from the Leones Valley (this study and Georgieva et al., 2016) likely discards the existence of a heat source in form of a shallow pluton in this area that could enhance the age pattern. Alternatively, a deeper source for a pluton (e.g., at the base of the lithosphere) is also unlikely as it would lead to higher dissipation of heat causing a broader anomaly with lower amplitude (e.g., Ehlers, 2005; Sibbett, 1988), decreasing the possibility to be detected by higher-temperature systems.

Therefore, we assume that the U-shaped distribution of observed thermochronometric ages across the study area is primarily controlled by tectonically induced differential exhumation, although additional effects of pre-existing topography and/or an elevated thermal gradients cannot be ruled out completely. In compressional tectonic settings such as the Patagonian Andes, thrust ramps are observed to produce high exhumation rates and U-shaped thermochronometric age patterns (e.g., Lock & Willett, 2008; McQuarrie & Ehlers, 2015). These patterns contain sharp transitions between young thermochronometric ages in the footwall and inherited older ages toward the foreland (including ages from high-temperature systems, e.g., Lock & Willett, 2008; Rak et al., 2017). Furthermore, similar steep gradients in thermochronometric ages

(U-shaped age pattern) are observed to be associated with strike-slip faulting, such as the LOFZ in the Northern Patagonian Andes (Thomson, 2002; Thomson et al., 2010) or the Giudiacare and Periadriatic faults in the Alps (Klotz et al., 2019; Pomella et al., 2012). In light of these observations, our hypothesis of tectonically induced, differential exhumation is reasonable. The decrease of thrusting in the retro-foreland of the Patagonian Andes (~30–15 Ma, e.g., Fosdick et al., 2011; Lagabrielle et al., 2004) and the onset of transpressive strike-slip faulting along the LOFZ (since 16–10 Ma, Cembrano et al., 2002; Thomson, 2002) temporally overlap with each other and correspond to the oldest reset thermochronometric ages (~8–14 Ma AHe, ~8–32 Ma AFT, ~8–20 Ma ZHe, and ~15 Ma ZFT, Tables 1 and S1, Figures S1 and S2), making it difficult to differentiate between these two tectonic drivers of rock uplift.

To test the hypothesis that reset thermochronometric ages in the study area are primarily controlled by pre-glacial, tectonically induced differential exhumation, we explore with numerical modeling which exhumation pattern(s) best explain the observed broad U-shaped distribution of thermochronological ages. Therefore, the modeling approach focuses first on finding the exhumation geometry, rates, and the basal temperature that best explains the observed regional (long-wavelength) spatial distribution of AFT, ZHe, and ZFT thermochronometric ages. We thus estimate the exhumation field active during the Middle to Late Miocene (following the main mountain building phase and activity of the LOFZ during the last 15 Myr). To do so, we conducted a series of experiments that included temporal and spatial variations in exhumation rate and magnitude. As all samples belong to the same stratigraphic unit (Cretaceous batholith), the effects of spatial variations in thermo-physical properties (volumetric radiogenic heat production, thermal conductivity, density, and heat capacity) on ages are not expected to be significant (e.g., Flowers & Ehlers, 2018).

Finally, we test the hypothesis that the Late Miocene glaciation (since ~7–5 Ma) caused accelerated exhumation. To do so, we focus on determining exhumation rates, onset and termination times that best explain the observed regional spatial distribution of the AHe ages. However, the effect of glacial erosion on exhumation can vary significantly in time and space over short wavelengths (e.g., two orders of magnitude within a 20-km-long catchment, Shuster et al., 2011), which is usually reflected by a spatially variable distribution of AHe ages (e.g., Ehlers et al., 2006) that we also observe in our area (Leones Valley). We estimate Late Miocene exhumation rates across short-wavelength topographic variations based on the spatial distribution of the thermochronometric ages in the Leones Valley. To disentangle exhumation controlled by the background tectonically induced rock uplift (controlled by activity along the LOFZ and the collision of the ridge segments, and/or slab window) and topographic changes driven by the erosional efficiency of the glaciers we use the iterative topographic reconstruction model of Olen et al. (2012, see Section 6.3). A stepwise increase in model-experiment complexity is presented below to demonstrate and filter out the controlling effects of the tested parameters on predicted thermochronometric ages.

5.2. Uniform Exhumation and Steady-State Topography (Simplest Scenario)

In this experiment, simulations started and ended with present-day (i.e., steady-state) topography, and a spatially uniform exhumation rate (Figures 5 and 6). We conducted 14 simulations that each include two time steps. The first time step covers the timeframe between 130 and 15 Ma. The onset of this time step corresponds to the oldest ZFT age in the study area (very close to the sample's crystallization age, Table S1). We set the exhumation rate to 0.15 mm/yr, which represents the average exhumation rate needed for the Cretaceous batholith, that was emplaced at ~20 km depth (Hervé et al., 1997), to reach the surface during the last 130 Myr. This time step represents a simplification of the Andean mountain-building phases that terminated at ~15 Ma (e.g., Fosdick et al., 2013; Lagabrielle et al., 2004 and references therein). The second time step covers the last 15 Myr. Here, we varied the exhumation rate from 0.2 to 1.5 mm/yr, at increments of 0.1 mm/yr between each simulation. This time step aims at simulating the latest exhumation phase postdating the major mountain-building phase. In all simulations, the basal temperature of 700°C is based on the crustal model of Tesauro et al. (2013). Details on thermo-physical properties used are listed in Table 2.

The best-fit scenarios show a cumulative χ^2 misfit of 25–26 (corresponding to a fit within 25–26 σ errors) for exhumation rates between 0.7 and 0.9 mm/yr (Figure 6a). A comparison of the best-fit scenarios for the thermochronometer systems considered here shows that different exhumation rates can be used to reduce χ^2 misfits for each thermochronometer system (Figure 6a). This suggests that more than one exhumation-rate

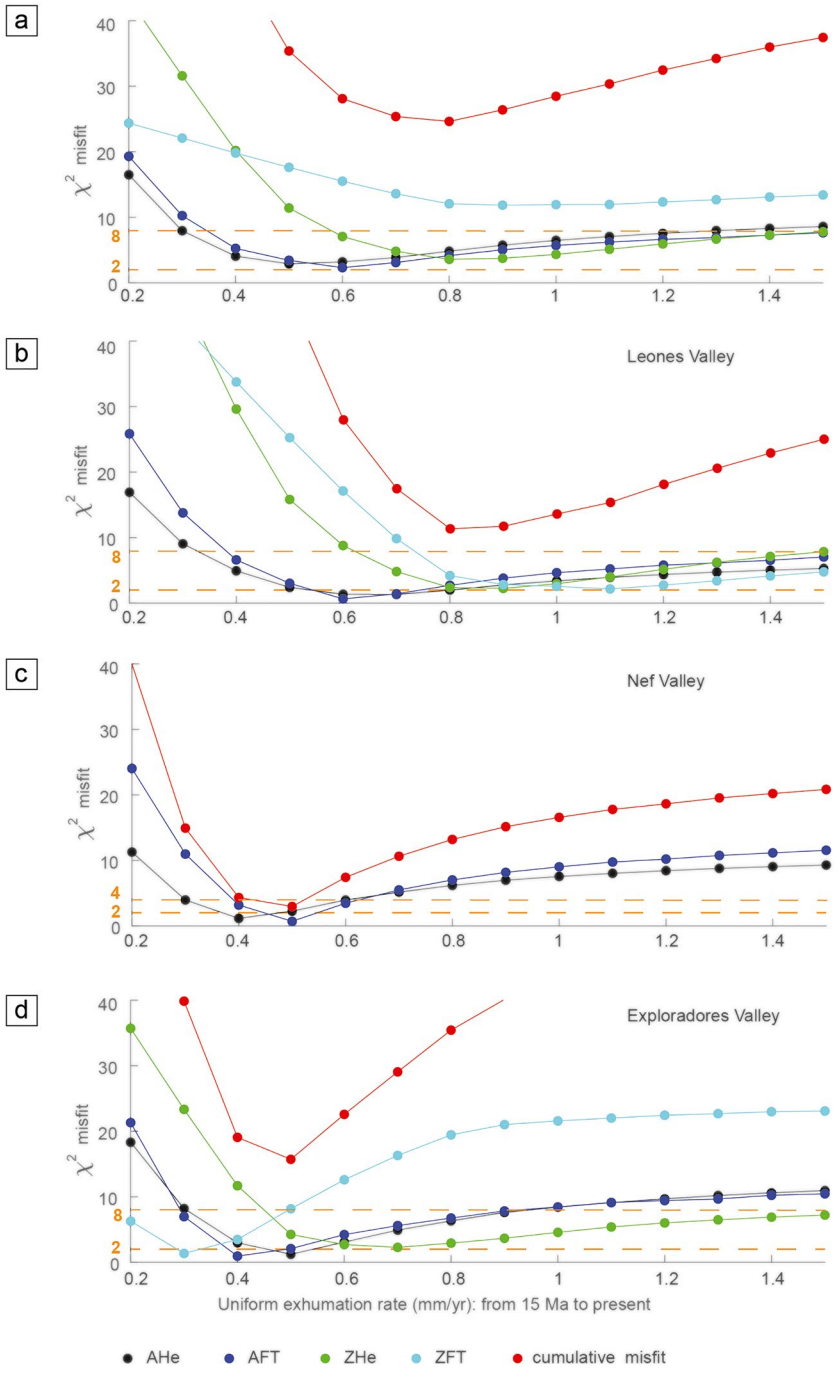

Figure 6. (a) χ^2misfit between predicted and observed thermochronometric ages for different uniform exhumation rates from 15 to 0 Ma. (a) χ^2 misfit for all samples in Figure 2, and misfit for subdomains shown in Figure 4 including (b) Leones, (c) Nef and (d) Exploradores valleys.

history can reproduce all thermochronometer ages. While scenarios with spatially uniform exhumation rates imposed on steady-state topography cannot reproduce the observed spatial variations in thermochronometric ages of all thermochronometric systems along the horizontal profile, the AHe and AFT (some ZHe, and ZFT) data of the elevation profiles in the Leones and Nef valleys are well-predicted (Figures 5, 6b, and 6c). For example, in the Leones Valley, exhumation rates of 0.6 mm/yr and 0.7 mm/yr produce minimum χ^2 misfits of 1–2 for AHe and AFT data (Figures 5c, 5e and 6b). However, these simulations fail to reproduce the increase in AHe ages at the lowest elevations (Figure 5c). Predicted ZHe thermochronometric ages require

exhumation rates between 0.8 and 0.9 mm/yr to produce a χ^2 misfit of 2 (corresponding to a fit within 2σ errors, Figures 5d and 6b). Although the same misfit allows an exhumation rate of 1.1 mm/yr, in the case of ZFT ages it only reproduces the observed younger thermochronological age at the base of the profile (Figures 5f and 6b). In the case of an older observed ZFT age (14.4 Ma, Table 1), the predicted age is ~7 Myr younger and requires a slower exhumation rate to be reproduced. In general, predicted ZHe and ZFT ages in the Leones Valley exhibit steeper age-elevation relationships compared to those observed (Figures 5d and 5f). This suggests that a spatially and temporally uniform exhumation history over the entire valley cannot explain the observed age-elevation trend in the case of higher-temperature systems.

Apatite (U-Th)/He and fission track ages from the Nef Valley (Figure 2d) are similarly well-predicted (χ^2 value of 1). The inferred values suggest an exhumation rate of 0.4 mm/yr and 0.5 mm/yr for AHe and AFT, respectively (Figures 5a, 5b and 6c). In the Exploradores Valley, apatite thermochronometric ages (both AHe and AFT) are well-predicted at a rate of 0.4 mm/yr (χ^2 value of 1–2, Figure 6d), whereas ZHe ages require rates of up to 0.6 mm/yr. These observations suggest that a spatial increase in exhumation rates of up to 0.1–0.2 mm/yr (accounting for AHe, AFT, and ZHe, Figures 6b–6d) in the Leones compared to the Nef and Exploradores valleys is required to reproduce the observed thermochronometric ages under the conditions dictated by these simulations.

Furthermore, the good fit ($\chi^2 < 2$) of AHe and AFT ages in these uniform exhumation and steady-state topography simulations shows that AHe and AFT closure-temperature isotherms (<110°C) mimic the overlying topography, suggesting that tectonic uplift and erosion (except samples <500 m from the Leones Valley defining a crescent shape) were mostly exhumed at the same pace and spatially constant during the last ~8–15 Myr (based on the oldest AFT ages in Exploradores, Nef and Leones valleys, Table S1). Note that this may be restricted only to elevations below ~2 km (as elevations of AHe and AFT samples are ≤ 2.1 km, Table S1).

Overall, model results show that a spatially and temporally uniform uplift field during the last 15 Myr cannot reproduce the regional U-shaped AFT, ZHe, and ZFT age patterns observed in the study area (Figures 2b and 2c), requiring a more complex model set up. In the next steps, we apply lessons learned (e.g., range of likely exhumation rates required) from the previous uniform uplift-rate scenario to develop a parabolic uplift field of variable size and location to explore the effect of a spatially variable exhumation field on predicted thermochronological ages. Furthermore, our model results show that the Leones Valley represents an area of anomalously high and variable local exhumation compared to the surrounding valleys (Nef and Exploradores), which likely resemble background exhumation rates. Therefore, data from the Leones Valley are processed separately (Section 5.4). Finally, we address the need for a temporal variation in the exhumation field in the Leones Valley by adding additional time steps to the chronology of changes in exhumation rates (Section 5.4).

5.3. Parabolic Exhumation Pattern and Steady-State Topography: Background Exhumation

In this section we focus on constraining the background-exhumation field in the study area. Based on the observed U-shaped patterns in thermochronometric ages and results from the previous section, we do this by exploring a parabola-shaped exhumation pattern. Simulations were designed to investigate the influence of: 1) the width and location of the parabolic exhumation pattern over the last 15 Myr; 2) the effect of exhumation rates and basal temperatures over the last 15 Myr; 3) variable onsets and rates of parabolic exhumation during the last 15 Myr; and 4) the effect of glaciation (last 7–5 Myr) simulated as a uniform exhumation field.

5.3.1. Effect of Width and Location of Parabolic Exhumation: 15 Ma to Present

We conducted 42 simulations to explore the effect of the width and location of the maximum exhumation rate (peak) of a parabolic exhumation field (cf. Figure 3b) on predicted ages during the last 15 Myr. The set of parabolic uplift-peak locations considered varied by increments of 5 km from 55 to 80 km measured from the center of the coordinate system of our model domain, located in the Golfo de Peñas (47°S, Figures 1 and 3). We tested parabolic exhumation-field widths of 40–160 km at increments of 20 km. Here, we focused on fitting the spatial distribution of the higher temperature systems (AFT, ZHe, and ZFT) and therefore use maximum exhumation rates of 0.6 mm/yr that provided a good fit to AFT, ZHe, and ZFT ages in the pre-

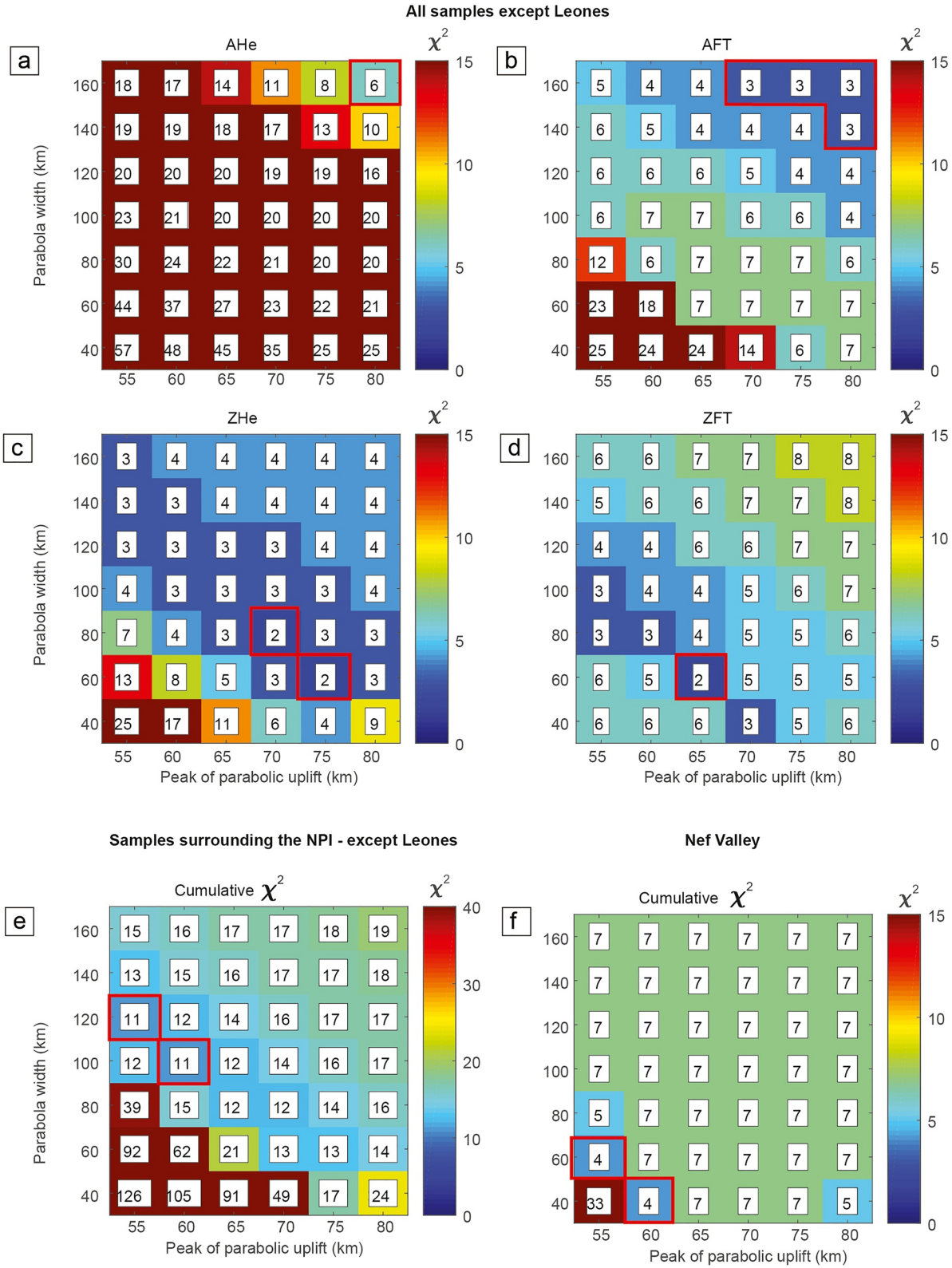

Figure 7. Effect of varying width and location of the maximum parabolic exhumation pattern (for the coordinate system see Figure 4a). (a–d) All samples except samples in the Leones Valley; (e) reset samples surrounding the Northern Patagonian Icefield (<100 km); (f) Nef Valley. Best-fit models identified are outlined by red lines.

vious experiment (cf. Section 5.2, Figures 6a and 6d). All other parameters remained equal to the best-fit model parameters from the previous experiment (cf. Section 5.2).

The results indicate the best-fit models for the AFT, ZHe, and ZFT systems (outlined by the red polygons in Figures 7b–7d) are achieved in different exhumation scenarios. Hence, an evaluation of this experiment based on the cumulative χ^2 misfit value for the entire data set would be misleading. The distribution of the average χ^2 misfit values for the AFT data shows a low sensitivity of predicted AFT ages to variations in the parabola peak location with increasing parabola width (Figure 7b). In contrast, the average χ^2 misfit values for the ZHe and ZFT systems show a linear dependence between the width of the parabolic exhumation field and location of the maximum exhumation rate (parabola peak; Figures 7c and 7d). This means that the observed ZHe and ZFT ages can be explained equally well by a wide parabolic exhumation field centered in the interior of the orogen (around the topographic divide of the NPI, e.g., 100–120 km wide parabola located at 60 km, Figures 2a and 7c, 7d) or a narrow parabola centered along the immediate eastern slopes of the NPI (e.g., a 40–60 km wide parabola at 70–75 km, Figures 2a and 7c, 7d).

This discrepancy between the ZHe and ZFT, and AFT data is expected given differences in the widths of the observed age patterns (Figures 2b and 2c), which cannot be reproduced using a single vertical parabolic exhumation field. Therefore, we focus on the area around the NPI, where all our reset AFT, ZHe, and ZFT ages capture the evolution of the area during the last 15 Myr (west of ~100 km, Figure 2a). In this region, the average χ^2 misfit values for each system show similar trends (Figure S3), implying that all thermochronometric systems could be explained by the same exhumation scenario. The reduced cumulative χ^2 misfit of 11 (Figure 7e) suggests that measured thermochronometric ages could be explained by applying a 120-km-wide parabolic exhumation pattern with peak-exhumation rate located at 55 km, or a 100-km-wide parabolic exhumation pattern with a peak at 60 km. These geometries lead to a good fit for AHe and AFT ages (χ^2 misfit of 2, Figure S3), while predictions of ZHe and ZFT ages are less accurate (χ^2 misfit of 3 and 4, respectively, Figure S3). The wide range of measured ZHe ages in the Exploradores Valley (~21–~9 Ma, Table 2) suggests a deviation in the real exhumation geometry from our modeled parabolic pattern. Therefore, we cannot find a better fit for ZHe ages (i.e., χ^2 misfit <2). The maximum exhumation rates of above 0.5 mm/yr (Figure 6c) fail to predict data from the Nef Valley (as shown in Section 5.2).

However, the reduced cumulative χ^2 misfit value suggests that increasing the maximum exhumation rate (from 0.5 mm/yr to 0.6 mm/yr used in this experiment) requires a narrower exhumation field to produce acceptable fits for the observed age-elevation profile (cumulative misfit of 4, which fits within 2σ error on average for each individual system, Figure 7f) in the Nef Valley. Except for the set of parameters outlined by the red polygon in Figure 7f, all other simulations overpredict observed ages by ~2–3 Myr.

Taken together, our preferred reference model describes a 100-km-wide parabolic exhumation field centered at 60 km that reproduces best the long-term background exhumation field. This geometry reproduces the steep age gradients from the NPI toward the east for all systems for samples at elevations <500 m (Figures 7 and S4). However, it poorly explains the observed age-elevation relationships observed in the Nef Valley (Figure 7f). Furthermore, it requires accelerated exhumation after ~7–6 Ma, possibly coeval with parabolic exhumation, in order to fit AHe ages farther east of the NPI (away from the influence of parabolic exhumation, Figure S4a) and youngest ZHe age in the Exploradores Valley Figure S4c).

5.3.2. Effect of Basal Temperature and Exhumation Rate: 15 Ma to Present

This sensitivity study is based on 36 simulations to evaluate the effect of variable basal temperatures and exhumation rates on predicted ages generated from our preferred parabolic exhumation geometry for the area around the NPI (width of 100 km, peak located at 60 km). Parabolic distribution of exhumation rates with the maximum rate ranging from 0.4 mm/yr to 1 mm/yr in increments of 0.1 mm/yr. Basal temperatures range from 400°C to 1,000°C in increments of 100°C. All other parameters were kept constant (Table 2).

Model results produced a minimum cumulative χ^2 misfit of 10, suggesting several possible solutions that are outlined in red in Figure 8a. This experiment shows that these combinations of maximum exhumation rate/basal temperature (i.e., 0.5 mm/yr/700°C, 0.6 mm/yr/600°C, and 0.7–0.8 mm/yr/500°C) produce slightly better model fits (misfit of 10 instead of 11, Figures 7e and 8) compared to our reference model. As expected, predicted thermochronometric ages from the Nef Valley show a better fit to observed ages under

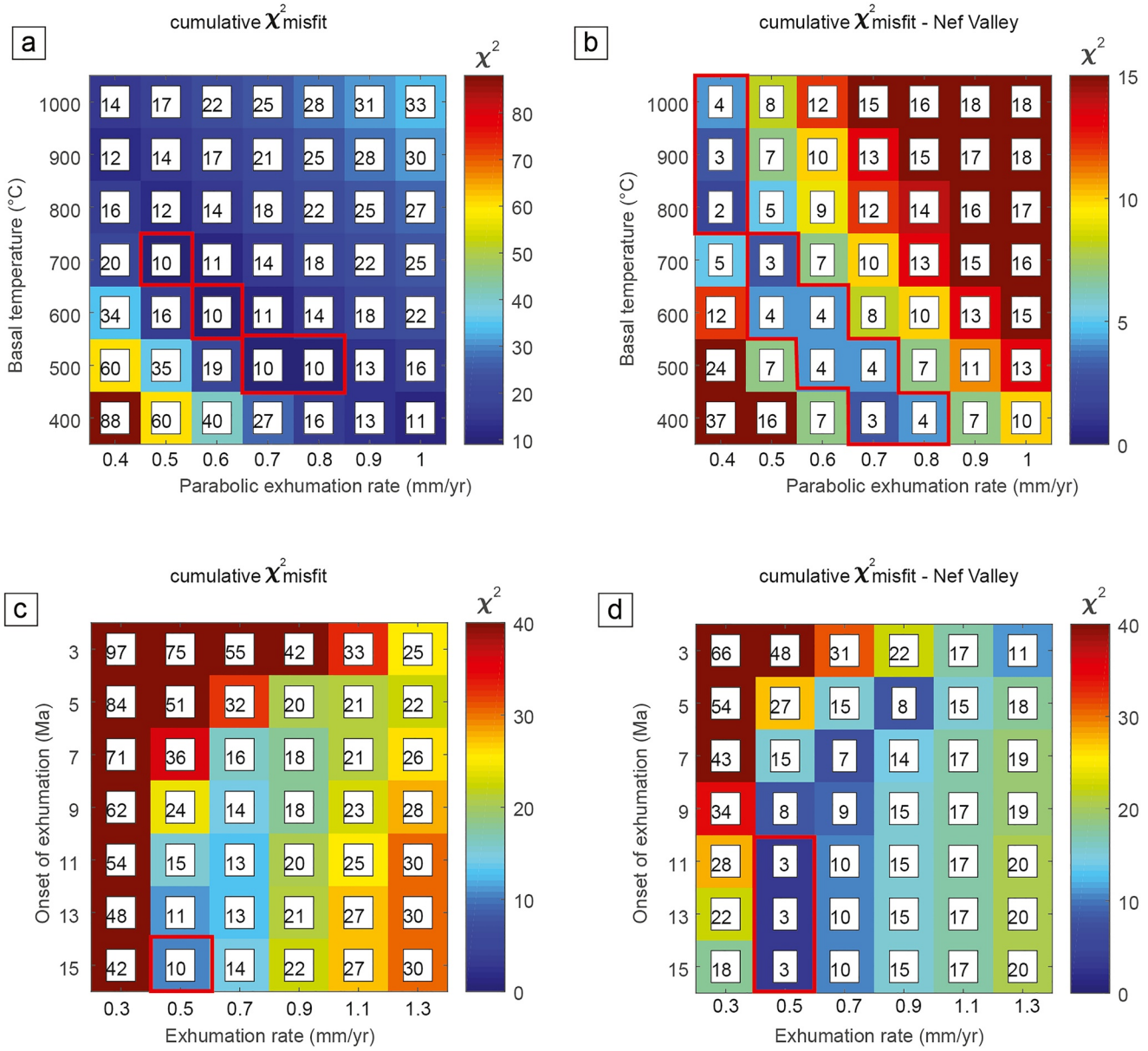

Figure 8. Effect of varying basal temperature and exhumation rates on all predicted thermochronometric ages for (a) samples surrounding the Northern Patagonian Icefield (NPI) and (b) in the Nef Valley. Effect of varying exhumation rates and onset time of the parabolic exhumation field on predicted ages for (c) samples surrounding the NPI and (d) in the Nef Valley.

lower exhumation rates and higher temperatures (e.g., 0.4–0.5 mm/yr and T > 700°C, Figure 8b), or higher exhumation rates and lower basal temperatures (0.6–0.8 mm/yr and 400–500°C, Figure 8b). It is noteworthy that an increase of the basal temperature or maximum exhumation rate does not significantly affect the first-order wavelength of the predicted ages in our reference model (exhumation rate of 0.6 mm/yr and basal temperature of 700°C, Figure S5). The increase in temperature and/or maximum exhumation rate will increase the amplitude of the age pattern and lead to variations in predicted ages. However, in contrast to variations in maximum exhumation rates where predicted ages are only affected by the exhumation rates prescribed within the exhumation pattern (i.e., parabola), the increase in basal temperature results in a general decrease of all predicted ages (Figure S5). In the following, we therefore retain a basal temperature of 700°C, as proposed by Tesauro et al. (2013).

5.3.3. Effect of Onset Time of Exhumation and Exhumation Rate: 15 Ma to Present

Here, we evaluate the sensitivity of the predicted thermochronometric ages to variations in exhumation rate and onset times of parabolic shaped exhumation. The maximum exhumation rates of the parabolic exhumation pattern range from 0.3 mm/yr to 1.3 mm/yr at increments of 0.2 mm/yr. Exhumation onset times varied from 15 Ma to 3 Ma at increments of 2 Myr. All other parameters were kept constant (e.g., parabolic exhumation pattern with a width of 100 km and a peak at 60 km, Table 2).

The reduced cumulative χ^2 misfits of 10 suggest that the observed thermochronometric ages can be best explained by a maximum exhumation rate of 0.5 mm/yr starting at 15 Ma (red rectangle in Figure 8c). The observed thermochronometric ages in the Nef Valley are reproduced by a maximum exhumation rate of 0.5 mm/yr (Sections 5.2 and 5.3.2, Figure 8d). The reduced cumulative $\chi 2$ misfit of 3 indicates a wider range of possible exhumation onset times (15–11 Ma, Figure 8d) compared to all other samples (Figure 8c).

5.3.4. Effect of Onset Time of Glaciation and Glacial Erosion Rate Increase

Here we investigate the hypothesis that glaciation caused an increase in erosion during the last 7 Myr. We use a uniform exhumation field to simulate erosion driven by glaciation in the entire model domain. In this section, a uniform erosion rate across the domain was used (rather than a parabolic field), because most of the observed AHe ages (Figure 2b, ~130–280 km) which record sample cooling over the last 2–13 Myr, correspond to the age of the onset of glaciation in the range; these ages do not show strong spatial variations and a U-shaped pattern (compare AHe and AFT ages, Figure 2b), and therefore would not be able to constrain a more complicated, spatially varying exhumation field. Furthermore, as the ice extent over the region (at least during the LGM) was extensive, it makes more sense to apply a uniform uplift pattern rather than spatially varying as in the previous sections. In the next section (Section 5.4), we investigate in more detail subtle variations (at the valley scale) in AHe age and here focus our attention on the regional pattern of observed AHe ages (Figure 2b) as they might relate to glacial erosion.

The tested onset times of glaciation ranged from 7 Ma to 1 Ma in increments of 2 Myr. The increases in erosion rate potentially due to glaciation ranged from 0 mm/yr to 1.5 mm/yr in increments of 0.5 mm/yr. The increase in erosion rates is imposed on an initial (pre-glacial) erosion rate of 0.5 mm/yr. All other parameters were kept constant (e.g., parabolic exhumation pattern with width of 100 km and peak at 60 km at rates from 15 Ma until the onset of glaciation defined in this experiment, Table 2). Although a comparison of all predicted and observed thermochronometer systems was carried out (e.g., Figure 6), the results presented here focus on the AHe system, which is most sensitive to recent changes in erosion rates, and for sample locations at <500 m elevation. Results indicate (Figure 9) that an increase in glacial erosion rates during the last 7 Myr produces an improved fit to observed AHe ages for samples with ages less than or equal to the on-

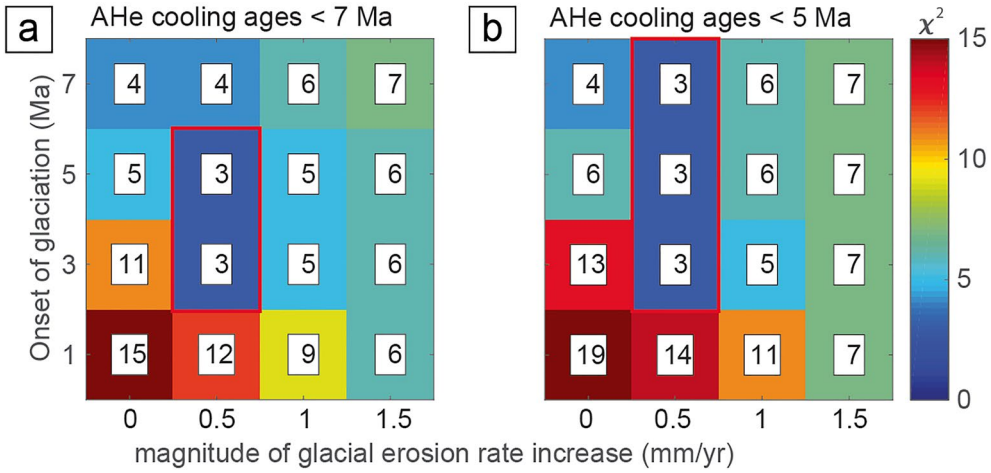

Figure 9. Effect of varying onset of glaciation and magnitude of the increase in glacial erosion on AHe thermochronometric ages (a) younger than 7 Ma and (b) 5 Ma.

set of glaciation. More specifically, for AHe ages less than 7 or 5 Ma (Figure 9), model predictions support an increase in erosion rates from the preglacial rate of 0.5 mm/yr to 1.0 mm/yr initiating in the last 7 to 3 Myr.

5.4. Parabolic Exhumation Pattern and Steady-State Topography: Leones Valley

Here we focus on constraining the pattern of exhumation in the Leones Valley. We do this because the observed AHe, AFT, and ZHe ages in this valley are the youngest observed in the study area (Figure 4) and suggest locally enhanced erosion may have occurred here relative to the Exploradores and Nef valleys to the north and south, respectively. The simulations conducted investigate the influences of: 1) the width of the parabolic exhumation pattern over the last 15 Myr; and 2) variable onset times and exhumation rates of the parabolic exhumation field during the last 15 Myr.

5.4.1. Effect of the Width of Parabolic Exhumation, Leones Valley: 15 Ma to Present

This experiment evaluates how spatial variations in the exhumation rate in the Leones Valley influence the age-elevation relationship of cooling ages. Here, we use a parabolic exhumation pattern with a peak of maximum exhumation located at 75 km (location of the sample with the youngest ZFT age, VG-11-LL-10, Table 1). The width of the parabola varied from 20 to 50 km at increments of 5 km. The maximum exhumation rate is 1.1 mm/yr corresponding to the best-fit model for ZFT ages in this area (see Section 5.2).

Only parabolic exhumation fields that are 35–40 km and 40–50 km wide provide a good fit to observed ZHe and ZFT ages (χ^2 misfits of 1–2, Figure 10a). Furthermore, a gradual decrease of the exhumation rate (parabolic exhumation pattern, Figure 10b) along the Leones Valley reproduces the observed ZHe and ZFT age-elevation relationship (Figure 10c) better than the uniform uplift (cf., Section 5.2, Figure 5d and 5f). Although parabolic exhumation patterns wider than 30 km generate similar age-elevation trends, as observed in the AHe and AFT data, most of the predicted ages are younger than the observed ages (Figure 10c). This suggests the need for a decrease or termination of the exhumation phase earlier than the present-day. In the final experiment we use a width of the parabolic exhumation pattern of 40 km that is, suggested by the reduced cumulative χ^2 misfit of 10 (Figure 10a), and explore the changes in exhumation rates leading to the present-day.

5.4.2. Effect of Duration and Rate of Parabolic Exhumation: 15 Ma to Present

This experiment adopts the best estimate for the long-term parabolic uplift geometry to explore transient model simulations with variable rate, onset, and termination of exhumation in the Leones Valley (Figures 11, 12 and S6). This set of simulations was conducted because the previous section (Figure 10c) indicates that in this valley constant rates of exhumation until the present predict younger than observed AHe and AFT ages. Results suggest that although an acceleration in erosion likely occurred coevally with glaciation (Section 5.3.4), AHe and AFT data in the Leones Valley (entire vertical profile) require a cessation, or slowing down of the exhumation rates in the recent past. We explore this by looking at a multistage exhumation history including a range of exhumation onset (at 15–3 Ma, at increments of 2 Myr) and termination times (9–1 Ma, at increments of 2 Myr), and a range of maximum exhumation rates (0.8–2.2 mm/yr, at increments of 0.2 mm/yr). This exhumation pulse is followed by a uniform exhumation rate of 0.1 mm/yr until present.

Several combinations of parameters yield a good fit to the observed thermochronometric ages in the Leones Valley (cumulative χ^2 misfit of 8 and lower, outlined in red in Figure S6). These simulations suggest maximum exhumation rates of 1.4 mm/yr and higher over the last 15–11 Myr. Moreover, the predicted ages exhibit a higher sensitivity to the onset and termination times of parabolic exhumation than to exhumation rates. As expected, higher maximum exhumation rates require shorter durations of exhumation, while lower maximum exhumation rates allow the exhumation phase to last longer. For example, the best-fit simulations for the maximum exhumation rate of 2.2 mm/yr requires exhumation to last for 8–10 Myr, starting between 13 Ma and 15 Ma and terminating no later than 5 Ma (Figure S6f), whereas a maximum exhumation rate of 1.4 mm/yr requires the phase to last for 12 Myr (15–3 Ma; Figure S6b). Although these examples show statistically good fits to the observed data (cumulative χ^2 misfit of 8), maximum exhumation rates higher than 1.6 mm/yr produce a steeper age-elevation trend than is observed in the Leones Valley

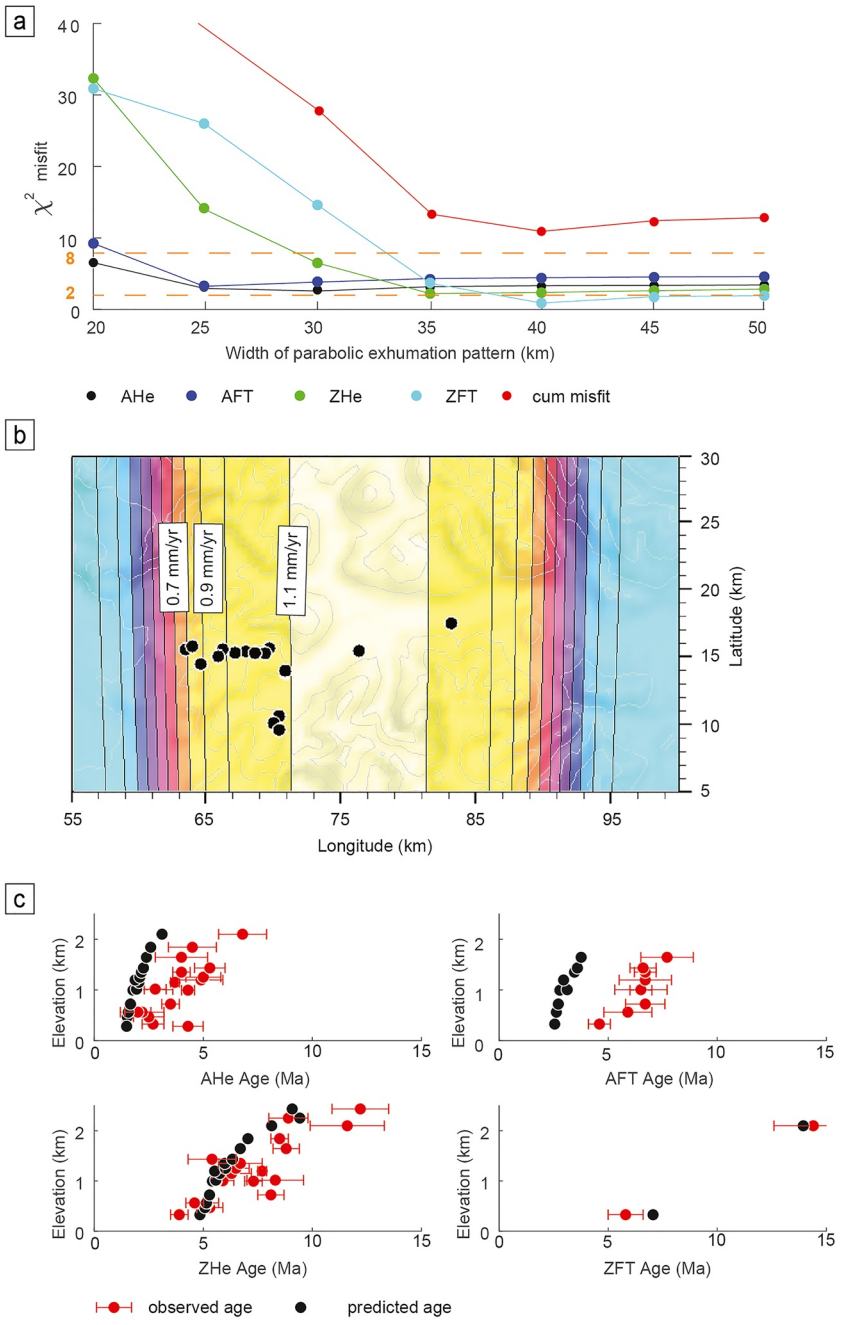

Figure 10. (a) Effect of varying short-wavelength parabola widths on predicted thermochronometric ages in the Leones Valley; (b) spatial variation in exhumation rate along the Leones Valley resulting from simulations where the width of the parabola was 40 km and the maximum exhumation rate of 1.1 mm/yr was located at 75 km. Black dots represent sample location. Gray lines are isolines; (c) age-elevation profile comparing observed and predicted thermochronometric ages for the exhumation scenario presented in (b).

(Figure 12). The lowest cumulative χ^2 misfit (7, outlined in red in Figure S6b) shows that simulations with an exhumation rate of 1.4 mm/yr and exhumation pulse lasting from 15 Ma to 3 Ma generate age-elevation profiles fitting the data within 1–2σ of sample uncertainties, on average (Figure 12). However, the results for the youngest AHe ages (elevations <500 m) still yield a poor fit to the data (underpredicted by 1–2 Myr, Figure 12). This suggests that the parabolic exhumation pattern incorporating unaltered present-day topography cannot reproduce these ages and an increase in erosion rates in the recent past is required. The χ^2 misfit

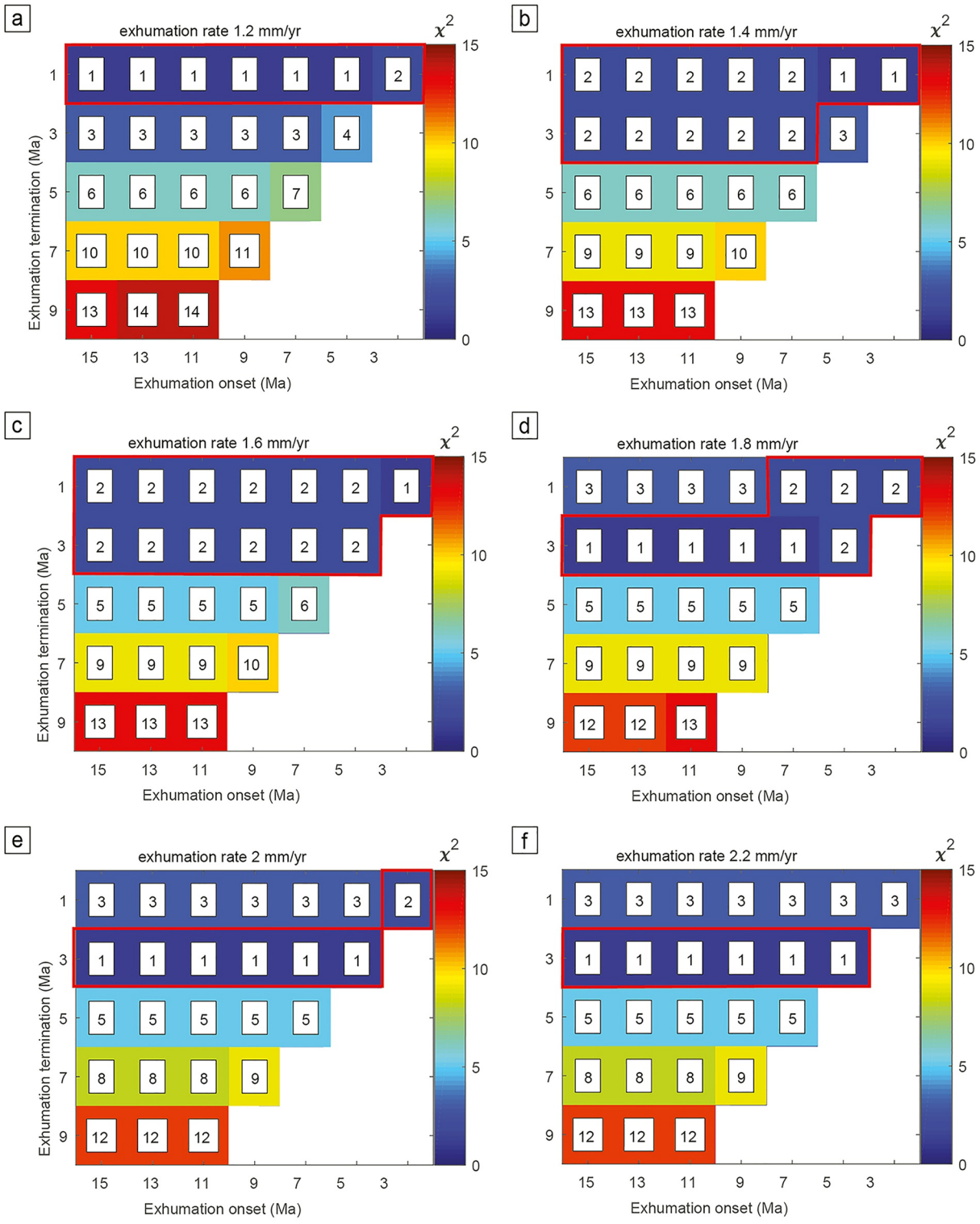

Figure 11. The χ^2 misfits evaluating the effect of exhumation rates, onset and termination of the exhumation on the fit of youngest AHe (younger than 5 Ma) observed in the Leones Valley at elevations <500 m.

calculated for the youngest AHe ages reveals that several transient exhumation scenarios provide improved fits to observed ages (Figure 11). Although our simulations suggest that the onset of exhumation could have occurred at almost any time investigated, the fact that observed thermochronometric ages are younger

than 5 Ma narrows down the possible scenarios to either: (a) a maximum exhumation rate of 1.2–1.8 mm/yr between 5–3 Ma and 1 Ma; (b) a maximum exhumation rate of 2–2.2 mm/yr between 5 and 3 Ma; or (c) a maximum exhumation rate of 2 mm/yr from 3 Ma until 1 Ma (Figure 11).

6. Discussion

Our new thermochronometric ages and model simulations allowed us to constrain the long-term, long- (orogen scale) and short- (Leones Valley scale) wavelength exhumation patterns in the Patagonian Andes at about 46.5°S. Furthermore, we identified a localized and shorter-term increase in exhumation coeval with Mio–Pliocene glaciation. In the following, we summarize evidence for widespread and localized exhumation in the study area and discuss potential controlling mechanisms.

6.1. Quantification of Long-Wavelength Exhumation

The model results demonstrate that the steep age-distance gradient observed in the thermochronometric ages from the vicinity of the NPI (Figures 2b and 2c) can be reproduced by imposing an orogen-perpendicular parabolic exhumation pattern (e.g., Figure S4). Our best-fit model suggests a 100-km-wide parabolic exhumation pattern with maximum and minimum rates of 0.5 and 0.1 mm/yr, respectively, averaged over the last 15 Myr. The highest exhumation rates corroborate previous findings from an elevation transect (Georgieva et al., 2016), and spatially overlap with the core of the orogen and the region of the highest topography in the NPI (Figures 2a, 7, and 13a).

The spatial distribution of exhumation rates suggested by our simulation results matches the deformation along the thrust front within the Andean retro-wedge east of the NPI (Figures 2d and 2e and 13a). We propose that thrust faulting, with subsequent offset on the LOFZ, were accompanied by efficient fluvial and glacial erosion and are likely mechanisms controlling the observed exhumation pattern during the last 15 Myr. Previous thermo-kinematic modeling studies in fold-and-thrust belts elsewhere (e.g., Lock & Willett, 2008; McQuarrie et al., 2019; McQuarrie & Ehlers, 2017) showed that exhumation associated with rock motion along mid-crustal ramps produces a characteristic U-shaped pattern of predicted thermochronological ages. Such thermochronometric age patterns have been observed in numerous fold-and-thrust belts around the world (e.g., Alps, Eizenhöfer et al., 2021; Hindukush, Kufner et al., 2016; Southern Alps, New Zealand, Batt et al., 2000), including the Southern Patagonian Andes (Fosdick et al., 2013).

In this type of tectonic setting, the horizontal translation of material along the thrust flat and out-of-sequence thrusting influence the skewness in the predicted thermochronometric ages. This is usually recorded by the lower temperature systems (AHe and AFT) as a U-shaped pattern with higher skewness in the direction of tectonic transport compared to the higher temperature systems (ZHe and ZFT, e.g., Lock & Willett, 2008; McQuarrie et al., 2019; Rak et al., 2017). This is also observed in our study area (Figures. 2b, 2c and S4). As our modeling approach includes only vertical exhumation, we were not able to simultaneously quantify the amount of vertical and lateral transport along the thrust system and fit observed AFT, ZHe, and ZFT age patterns (see Section 5.3.1). Considering the observed reset AFT ages, out-of-sequence (westward) propagation of the exhuming zones probably occurred between ~30–28 Ma and ~10 Ma (Table 1, Figures. S1 and S2). This timeframe corresponds to the main mountain building phase and increased sediment flux in the retro-foreland Magallanes-Austral basin (~30–12 Ma) of the Patagonian Andes south of 47°S (Encinas et al., 2019; Folguera et al., 2018; Fosdick et al., 2011, 2013; Ramos, 1989; Thomson et al., 2001).

To the west of the crest of the Andes, the W–E concave-upward thermochronometric age distribution is truncated (or displaced) by the LOFZ (Figure 2) suggesting a potential effect of transpression-related rock uplift on the observed age patterns (Georgieva et al., 2016, 2019; Schildgen et al., 2018). Certainly, the collision of the ridge segments over the last ~6 Myr associated with the activity of the LOFZ could lead to spatial and temporal variations in stresses and topographic growth in the area of the NPI (between 46°S and 47°S, Figure 1), also suggested by Georgieva et al. (2016). The NPI topography shows typical features of restraining bends in transpressional zones (e.g., Cunningham, 2007), such as: (a) elongated to sigmoidal strands of higher topography; and (b) a thrust fault that formed perpendicular to the principal compressive stress (Exploradores thrust, Figures 2 and S1b, Georgieva et al., 2016). Restraining bends are often characterized

by patches of accelerated vertical uplift over relatively short along-strike distances and short timescales (up to 2.3 mm/yr for 5 Myr, Fattaruso et al., 2014), which are not represented in our models. Although such a geometry might be able to reproduce the latitudinal variations in observed thermochronometric ages between valleys flanking the NPI (Leones, Nef, Exploradores, Figure 4; Georgieva et al., 2016, 2019), it alone cannot explain the observed long-term exhumation pattern in the study area as reset ZHe ages of ~20–18 Ma (Table 1) predate the LOFZ activity (since ~16–10 Ma, Cembrano et al., 1996, 2002; Thomson, 2002).

6.2. Quantification of Short-Wavelength Exhumation

The model simulations restricted to data from the Leones Valley confirm a long-term (between 15–11 Ma and 5–3 Ma, Figures 10b and 12 and S6) valley-scale parabolic exhumation pattern that predates glaciation. Although our best-fit simulations for the Leones Valley (Figure S6b–f) show a decrease in exhumation rates (at the valley scale, averaged during the last 15 Myr) from 1.4 mm/yr to 0.1 mm/yr sometime after 5–3 Ma, the transient exhumation histories for the lowermost (<500 m, Figure 2b) and youngest (younger than 5 Ma) AHe ages provide improved fits to observed thermochronometric ages in the case of accelerated localized exhumation during the last 5–3 Myr (Figure 11). This result differs from the work of Christeleit et al. (2017) who suggested an acceleration in glacial erosion in Southern Patagonian fjords between 10 and 5 Ma, followed by a decrease in rates. Our suggested timing for a decrease in rates (averaged over the entire Leones Valley) to 0.1 mm/yr at ~5–3 Ma, rather than 7–5 Ma, could be the result of either the difference in geographic location, or our analysis of samples obtained close to valley bottoms (<500 m). The thermochronometry samples interpreted in Christeleit et al. (2017) were collected above sea-level in fjords and did not cover locations at the fjord bottom where more efficient glacial erosion would be expected. This suggests that erosion rates in Patagonia may have increased close to the onset of glaciation (~7–5 Ma) and then decreased between 5 and 3 Ma coeval with Late Pliocene and Quaternary glaciations, which is also suggested by C. D. Willett et al. (2020). We note that previous glacial landscape-evolution modeling of oscillating glacial/interglacial conditions predicts the same behavior in erosion histories as observed here (Yanites & Ehlers, 2012). For example, predicted erosion rate histories over multiple glacial/interglacial cycles suggest glacially accelerated rates during initial glaciations that are superseded by an overall decrease in erosion. The acceleration of glacial erosion during the onset of glaciations is often related to the changes in valley hypsometry due to its transition from a fluvial ("V") to a glacial ("U") valley shape and the changing elevations (and subsequently temperatures) at which subsequent glaciations can form ice (Prasicek et al., 2015; see Figure 4 of Yanites & Ehlers, 2012).

The higher-temperature (ZHe and ZFT) thermochronometer data obtained in our study area suggest a gradual eastward and downslope increase in erosion rates within the valley (Figure 10b). In contrast, the lower-temperature systems (AHe and AFT, Figures 5c and 5e, except for the youngest AHe ages) can be reproduced equally well by applying a temporally and spatially uniform (vertical) exhumation field. This difference in spatial variations in the exhumation rate between these high and low-temperature systems can be explained by different mechanisms (tectonic vs. glacial) exerting a dominant control on observed thermochronometric ages at different times in the exhumation history of the study area. For example, the parabolic exhumation field identified here (e.g., Figure 10) provides the best fit with higher-temperature systems (ZHe and ZFT). As previously discussed, this exhumation field is most likely the consequence of a crustal ramp at depth. In contrast, observed low-temperature ages over long wavelengths from the range crest to the foreland are more uniform (Figure 2), and as a result are most easily interpreted by a uniform erosion rate across the region (Figures 6a and 9) resulting from glaciers that covered the area.

However, the glacially induced uniform erosion pattern (Section 5.3.4) is superimposed by shorter-wavelength variations (valley scale, Leones Valley) in exhumation rates. Although uniform exhumation in the Leones Valley cannot be entirely ruled out, the poor fit for the youngest AHe ages (from samples at <500 m, Figures 5c and 5e) implies some degree of differential incision whereby valley bottoms experience higher exhumation rates than ridge crests. The χ^2 misfits show that several transient exhumation histories involving accelerated exhumation of 1.2–2.2 mm/yr during the last 3–5 Myr improve the fit to the observed lowermost and youngest AHe data (Figure 11). Assuming no other sources of local thermal perturbations, such as shallow plutons or local faulting causing differential uplift and exhumation within the Leones Valley, the proposed localized increase in glacial erosion of pre-existing topography during the Plio-Pleistocene is

the most plausible explanation. This is supported by the coincidence of the elevation of the youngest AHe ages and the LGM ELA (~500 m), which corresponds to the region of most efficient glacial erosion in catchments, as supported by previous modeling studies (e.g., Herman & Braun, 2008; Tomkin & Braun, 2002; Yanites & Ehlers, 2012, 2016).

6.3. Disentangling Tectonic and Glacial Contributions to the Topographic Evolution of the Patagonian Andes During the Late Cenozoic

In glaciated and tectonically active mountain belts, such as the Patagonian Andes, the topographic evolution involves competing effects of tectonic rock uplift, climatic gradients (e.g., variations in temperature and precipitation rates across and along strike of the mountain belt), and glacial and fluvial erosion over short and long wavelengths (e.g., Berger et al., 2008; Mitchell & Montgomery, 2006; Pedersen et al., 2014; Whipple et al., 1999). We have shown that the distribution of thermochronometric ages from the Southern Patagonian Andes at the latitude of the NPI contains signals of both long-term tectonic processes and more recent glacial modification of topography.

Specifically, tectonic effects are reflected by the E–W U-shaped distribution of thermochronometric ages across the orogen (Figure 2). This pattern can be explained by a parabolic exhumation field (Figures 7 and S4), which temporally and spatially corresponds to Late Cenozoic thrusting and subsequent transpression. As we were able to fit most of the observed thermochronometric ages using our steady-state topography modeling approach, this suggests that the general long-wavelength pattern of topography is long-lived (at least over the last 15 Myr) and thus was similar to the present-day. This is supported by the correlation between our preferred modeled exhumation pattern and elevation (mean and max, Figure 13a) and by the paleoenvironmental evolution of Patagonia associated with formation of topography as an orographic barrier (Blisniuk et al., 2005; Hinojosa & Villagrán, 1997). This means that the upward motion of rocks above a crustal thrust ramp, and subsequent transpressional faulting along the LOFZ, created high topography in our study area. This interpretation is consistent with other studies that suggested high topography in the Patagonian Andes south of 49°S is controlled by thrust faulting in the retro-wedge (Fosdick et al., 2013; Ramos & Ghiglione, 2008). The correspondence between high topography and a thrust front is commonly observed in doubly vergent orogens worldwide (e.g., Pyrenees, Southern Alps in New Zealand, Southern Patagonian Andes; Batt et al., 2000; Fosdick et al., 2013; McQuarrie & Ehlers, 2017).

Based on the across-strike distribution of thermochronological ages in the Patagonian Andes south of 46°S (Fosdick et al., 2013; Georgieva et al., 2016, 2019; Guillaume et al., 2013; Thomson et al., 2010), we note that tectonically induced exhumation in the retro-wedge prevails in the recorded AFT, ZHe and ZFT thermochronometric ages over the climatically induced exhumation driven by west-east climatic gradients (Blisniuk et al., 2005) over the last 15 Myr. This means that since the establishment of the orographic precipitation pattern across the Patagonian Andes (~16–14 Ma, Blisniuk et al., 2005), the windward (wet, western) side of the orogen experienced less exhumation compared to the dry, but tectonically active side (this study; Fosdick et al., 2013). This implies a small influence of W–E climatic gradients on the long-wavelength topography and its amplitude during the last 15 Myr.

The Late Cenozoic cooling and the onset of glaciation at ~7–5 Ma (Mercer & Sutter, 1982; Ton-That et al., 1999) in the study area was conducive to the creation of short-wavelength topography (e.g., U-shaped valleys, hanging valleys, and cirques) observed today. While in numerous other glaciated orogens, Late Cenozoic cooling appears to have been associated with an overall acceleration in exhumation (e.g., Berger et al., 2008; Herman et al., 2013; Michel et al., 2018), we recorded long-term exhumation in our study area predating glaciation on the valley scale (Figures 8c and 8d, 10, 12 and S6, cf., also Georgieva et al., 2016). However, if we take into account the sparse remains of moraines (~49°S, Wenzens, 2006) and fluvioglacial conglomerates (~45–46°S, Suarez et al., 2007) that suggest an earlier onset of glaciation at about 10 Ma (Wenzens, 2006) or even extending back as far as the Middle Miocene (Suarez et al., 2007; ~12 Ma–R. De la Cruz, M. Suarez, M. Fanning pers. comm. to Lagabrielle et al., 2010), the recorded long-term exhumation might also be controlled to some extent by glaciation, although we are not able to resolve a signal of this in the higher-temperature thermochronometric ages.

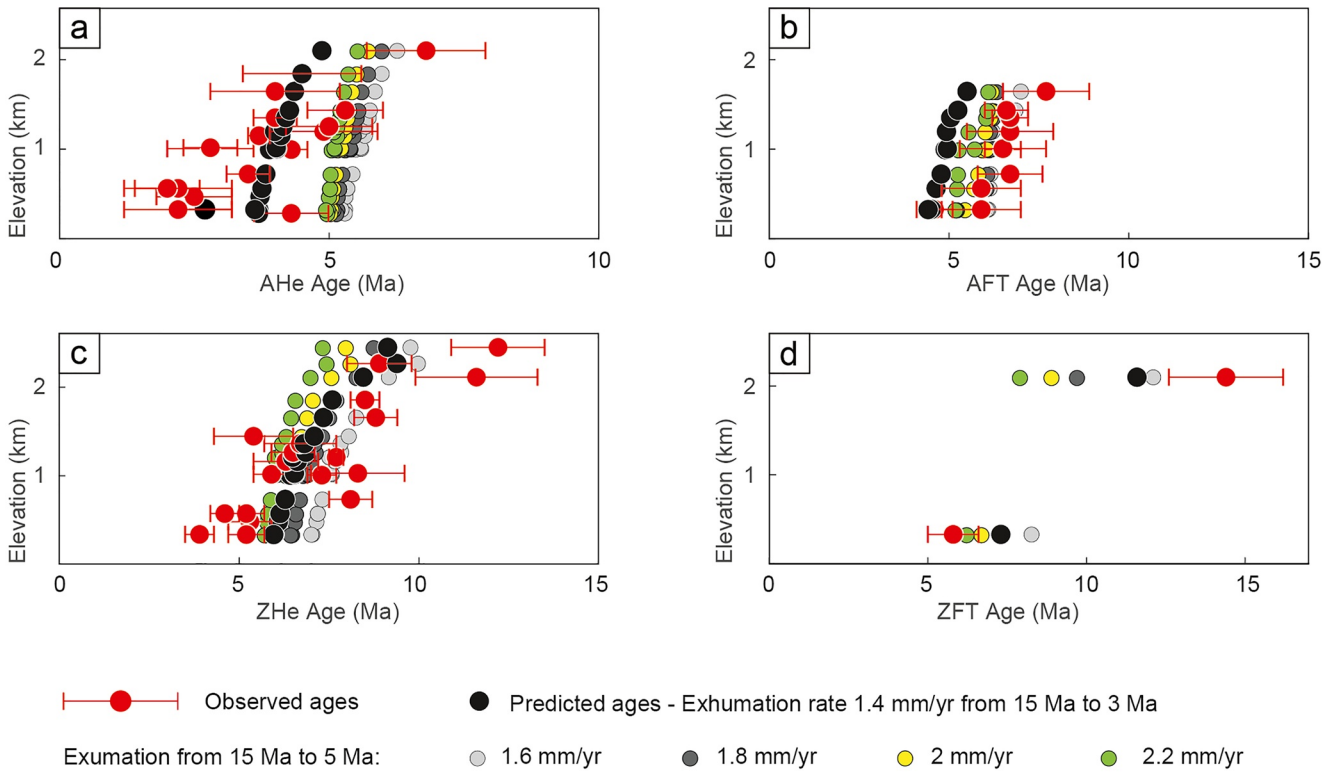

Figure 12. Age-elevation relationships comparing observed and predicted thermochronometric ages for variable parabolic exhumation rates and durations.

The impact of glaciation on the exhumation history of the region is most evident in the lower-temperature AHe data. More specifically, we find from simulations using uniform uplift and acceleration in exhumation rates (Section 5.3.4) non-U-shaped, or almost flat lying, patterns of AHe ages (~130–290 km, Figure 2b) that suggest a regional acceleration of exhumation rates occurred sometime in the last ~7–5 Myr, which is coeval with the onset of glaciation. However, despite the regional acceleration in exhumation rates at this time, more subtle spatial variations in glacial erosion may be present at the catchment scale. For example, in the Leones Valley, model results detected a glacially induced change in topography, likely induced by glacial incision during the last 5–3 Myr. The location of this accelerated exhumation (green parabola in Figure 13b) coincides with a shift in the trend of mean and maximum local relief (dashed and solid red lines in Figure 13b, respectively) and the mean and maximum elevations (dashed and solid black lines in Figure 13b, respectively). We find that decreases in the mean and maximum elevations correspond with increasing mean/maximum local relief (outlined by the orange ellipse in Figure 13). We interpret this as another indication of a transient topographic signal resulting from disequilibrium between rock uplift and glacial erosion (e.g., Brocklehurst & Whipple, 2007). However, in the future, as a consequence of this process, both the relief and elevation of the study area will likely be reduced due to the tendency to concentrate the mean elevation around the ELA, which is commonly referred to as the "buzzsaw effect" (e.g., Brozović et al., 1997; Mitchell & Montgomery, 2006; Shuster et al., 2011).

The previous discussion highlights that although tectonic processes are responsible for the formation of long-wavelength topography and higher-temperature thermochronometric ages in this region, the initiation of glaciation sometime in the last 7 Myr induced a change in the pattern of AHe ages. To quantify the potential effect of glaciation on topography we applied the approach of Olen et al. (2012) to iteratively solve for the range of linear topographic changes required to produce an improved fit (χ^2 misfit ≤2) to the observed AHe ages in the Leones Valley (Figure 14). This approach is based on the assumption that the entire misfit between observed and predicted AHe ages is produced by changes in topography. Therefore, we use the simplest geological scenario and simulate topographic change due to glacial erosion as a single event (averaging all glacial cycles during the last 7 Myr). To do this, simulations were conducted in 3D with a

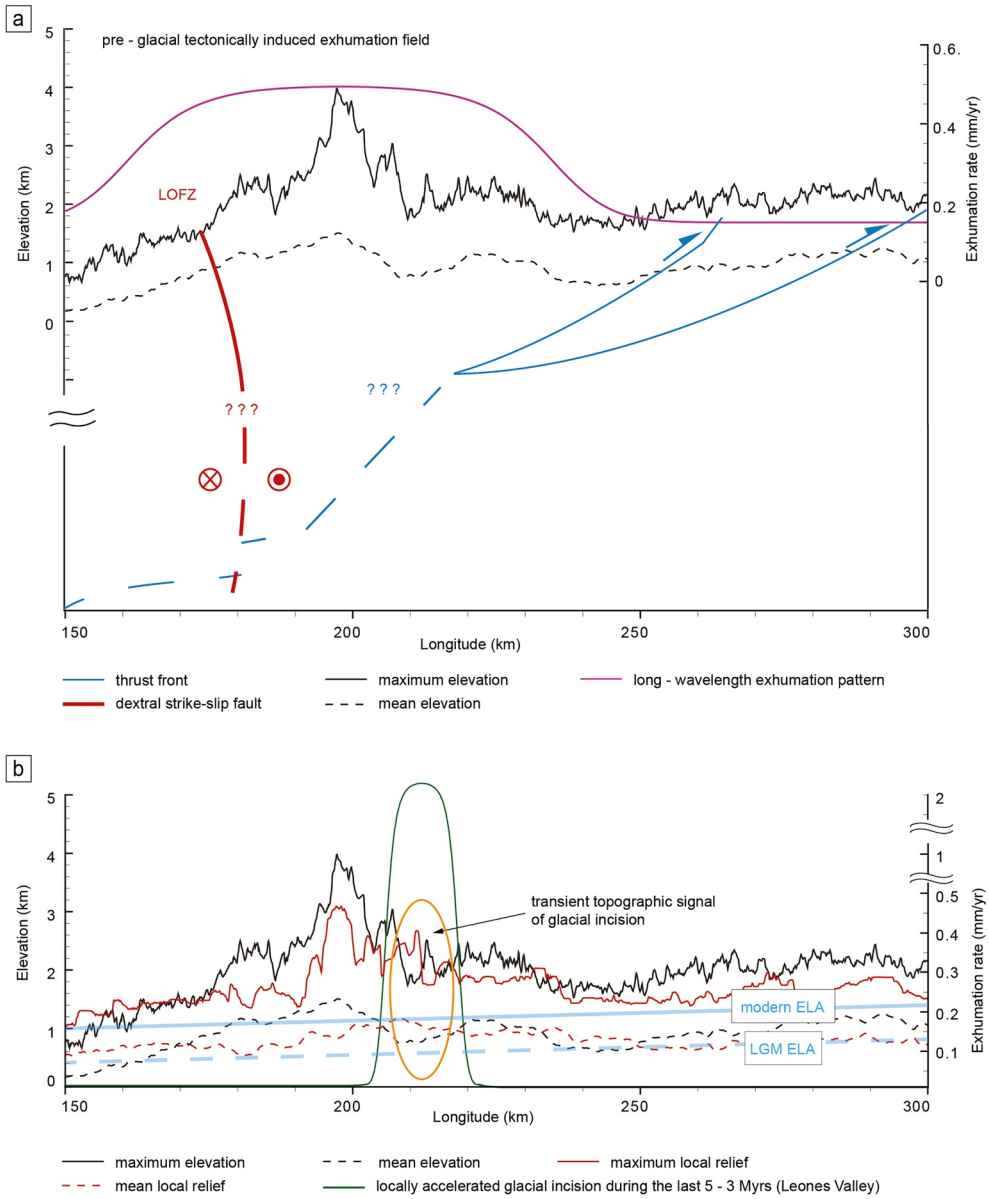

Figure 13. Swath profile of the area east of the Chile Triple Junction with mean and maximum elevation and local relief. (a) The predicted long-wavelength exhumation pattern (pink parabola, generated by our best-fit model, for details see Section 5.3) represents the cumulative effect of thrusting (blue line, both solid, and dashed) and subsequent strike-slip (red line, both solid and dashed) faulting during the last 15 Myr. Following previous thermokinematic modeling studies (e.g., Lock & Willett, 2008; McQuarrie & Ehlers, 2017) we used the highest exhumation and lowest reset thermochronometric ages (see also Figures 2b and 2c and Section 6.1) to infer thrust geometry, that is, location of the deep-seated ramp(s?), shown in the blue dashed line) in the study area. (b) The predicted short-wavelength exhumation pattern (green line) represents the long-term erosional response at the valley scale to regional tectonic activity. A glacially induced transient topographic signal is represented by the shift in the elevation and relief trends (orange ellipse, see also Section 6.3 for details). The distribution of the mean and maximum local relief are created by calculating the maximum difference in elevation within a 5 km diameter moving window (for details see also Adams & Ehlers, 2017). The modern and Last Glacial Maximum (LGM) equilibrium-line altitude (ELA) are from Rivera et al. (2007).

parabolic background (tectonically driven) maximum exhumation rate of 0.5 mm/yr for the initiation phase prior to 7 Ma. From 7 Ma to the present, we imposed uniform background (tectonically driven) exhumation rates between 0.2 and 0.5 mm/yr. All simulations were conducted with a basal temperature of 700°C, and

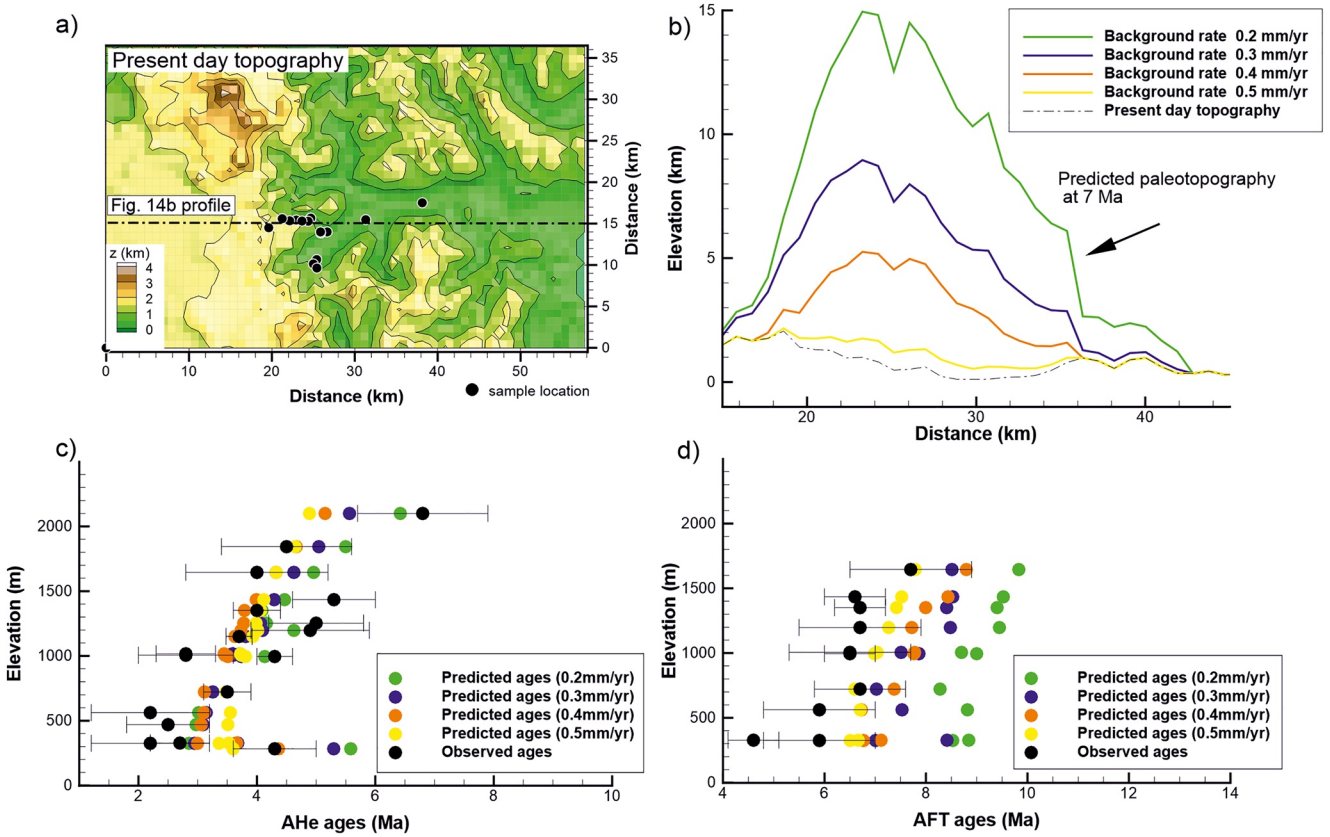

Figure 14. Model results for simulations considering paleotopographic change from 7 Ma to the present. Simulations follow the iterative topographic inversion approach of Olen et al. (2012) and build upon the best-fit simulations presented in previous Sections 5.3.3 and 5.3.4. (a) Present day topography and AHe sample locations used in simulations. (b) Reconstructed paleotopographies at 7 Ma required to minimize the misfit to observed AHe ages for different background exhumation rates (see text for discussion of unrealistic paleotopographies shown). (c) Predicted and observed present-day AHe age-elevation relationships for different background exhumation rates. The shape and slope of each model prediction vary depending on the evolution of paleotopographies shown in part (b) toward present-day. (d) Predicted and observed present-day apatite fission track (AFT) age-elevation relationships for paleotopographic change scenarios shown in part (b).

thermophysical properties identical to those used in previous simulations (see Section 5.3.4). Thus, the only parameter changing in these simulations was the uniform background exhumation rate.

It should be noted that in this type of approach, there is a non-uniqueness in predicting AHe ages implying that the observed AHe ages could be equally well explained either by higher uniform background exhumation rates and lower changes in topography or lower uniform exhumation rates and higher changes in topography. Thus, all of the resulting paleotopographic profiles shown in Figure 14b fit the observed AHe ages, but some make more geologic/geomorphic sense than others. For example, at a uniform background exhumation rate of 0.2 mm/yr (slower than the 0.5 mm/yr suggested in previous sections prior to 7 Ma) an unrealistic paleotopographic high of ~15 km elevation is required to produce high enough exhumation rates to minimize misfits to the AHe data. In contrast, at a higher background exhumation rate of 0.5 mm/yr (equal to the best-fit exhumation rate prior to 7 Ma suggested in previous sections) a smaller topographic change (on the order of ~100 m) is required to minimize the AHe age misfit. Both scenarios (0.2 vs. 0.5 mm/yr uniform background exhumation rate) produce reasonable AHe age-elevation relationships within sample uncertainties (Figure 14c).

It is challenging to narrow down which topographic change and uniform background exhumation rate scenario are most likely because the signal of paleotopography in the AHe ages is weak, and can almost be fitted by constant exhumation of 0.5 mm/yr over the last 7 Myr with steady-state topography (Figure 14b, yellow curve). The non-uniqueness in solutions can be addressed by looking at thermochronometer systems with higher closure temperature such as AFT (Figure 14d). For the topographic reconstruc-

tions presented in Figure 14b, only those with a uniform background (tectonically driven) exhumation rates of 0.5 mm/yr and 0.4 mm/yr provide the best fit to AFT ages within sample uncertainties. As a result, we propose the two following scenarios: (a) uniform background exhumation rates from 7 Ma to present either stayed the same as before 7 Ma and minor (on the order of 100 m, yellow curve, Figure 14b) changes in topography occurred from accelerated glacial erosion rates. Alternatively, (b) exhumation rates from 7 Ma to present were slightly decreased (from 0.5 to 0.4 mm/yr) and topography decreased by about 4.9 km (orange curve, Figure 14b) from 7 Ma to present due to significantly enhanced erosion rates from glaciation. We consider the later scenario (b) more likely (a decrease in tectonically driven background rock uplift) because as discussed previously, other lines of geologic evidence suggest a decrease in tectonic processes contributing to rock uplift in the last 7 Myr and a change in deformation style from thrust faulting toward more transpressive behavior.

In summary, taking the higher- and lower-temperature data together, we find that long- and short-wavelength exhumational pattern and topography were controlled by the long-term erosive response to variations in regional tectonics that predated glaciation. It is noteworthy that our exhumation rates are averaged over timescales of 10^6–10^7 years and could contain shorter exhumation pulses which are not resolvable (e.g., S. D. Willett et al., 2020). Such pulses could be potentially driven by the regional and local climate variations and may be expressed only locally, such as observed in the Leones Valley (1–3 Myr long pulses). This is consistent with previous studies (Ramos & Ghiglione, 2008) favoring the hypothesis of a strong tectonic influence on exhumation and topography development in the Southern Patagonian Andes. Thus, although this study supports that Pleistocene glaciation recently enhanced erosion rates (e.g., Herman et al., 2013; S. D. Willett et al., 2020), we find that the large-scale spatial pattern of exhumation and long-wavelength topography primarily reflect tectonic processes.

7. Conclusions

The new AHe, AFT, ZHe, and ZFT data, and 3D thermo-kinematic modeling results presented in this study quantify long-term and short-term changes in exhumation rates and topography during the last 15 Myr in the Southern Patagonian Andes at 46.5°S. Our new data and numerical model results suggest that an observed spatial gradient in AFT, ZHe, ZFT thermochronometric ages requires a 100 km-wide parabolic-shaped regional exhumation pattern with an average maximum rate of 0.5 mm/yr located in the vicinity of the Northern Patagonian Ice field and active during the last 15 Myr. Our exhumation pattern coincides spatially and temporally with thrusts and strike-slip faults associated with the Liquiñe-Ofqui Fault and likely records thrust- and transpression-related rock uplift coupled with surface processes in the retro-wedge domain. Furthermore, our modeling study shows that tectonically induced rock uplift drove the development of the long-wavelength topography and created high elevation topography during the last 15 Myr.

Analysis of the low-temperature AHe thermochronometric data and numerical simulations demonstrate that glaciers caused an up to twofold (from the preglacial rate of 0.5 mm/yr to 1.0 mm/yr) increase in average regional and spatially uniform exhumation rates during the last 7–3 Myr. Locally, on the valley scale (Leones Valley), our findings reveal that the youngest AHe ages (<5 Ma) record transient glacial erosion rates that may be up to 2.2 mm/yr, demonstrating an up to fourfold increase in erosion rates during the last 5–3 Myr.

Similar to results from studies in other mountain ranges worldwide, we find that the most efficient glacial erosion occurred near the ELA. In contrast to the pre-glacial exhumation phase, glacial erosion rates caused a regional acceleration in exhumation. In addition, our high data density allows us to conclude that shorter-wavelength (valley scale) spatial variations in accelerated erosion are superimposed upon this regional trend in local areas (Leones Valley).

Data Availability Statement

Data have been archived at https://doi.org/10.5880/fidgeo.2021.004.

Acknowledgments
This study was supported by DFG grants to Todd Ehlers (EH329/18-1) and Manfred R. Strecker (STR 373/37-1). Viktoria Georgieva's co-authorship was supported by DFG grant STR 373/37-1 and the Chilean Government ANID/FONDECYT Postdoctoral Grant 2020 °N3200375. We thank Associated Editor Mikaël Attal and Matthew Fox, Ruohong Jiao and two anonymous reviewers for constructive comments that substantially improved the quality of this manuscript.

References

Adams, B. A., & Ehlers, T. A. (2017). Deciphering topographic signals of glaciation and rock uplift in an active orogen: A case study from the Olympic Mountains, USA. *Earth Surface Processes and Landforms*, *42*(11), 1680–1692. https://doi.org/10.1002/esp.4120

Andrić-Tomašević, N., Falkowski, S., Georgieva, V., Glotzbach, C., Strecker, M. R., & Ehlers, T. A. (2021). Supporting material for Quantifying tectonic and glacial controls on topography in the Patagonian Andes (46.5°S) from integrated thermochronometry and thermokinematic modeling. *GFZ Data Services*. https://doi.org/10.5880/fidgeo.2021.004

Angermann, D., Klotz, J., & Reigber, C. (1999). Space-geodetic estimation of the Nazca-South America euler vector. *Earth and Planetary Science Letters*, *171*(3), 329–334. https://doi.org/10.1016/S0012-821X(99)00173-9

Astudillo-Sotomayor, L., Jara-Muñoz, J., Melnick, D., Cortes-Arnda, J., Tassara, A., & Strecker, M. R. (2021). Fast Holocene slip and localized strain along the Liquiñe-Ofqui strike-slip fault system. *Chilean Scientific Report*, *11*, 5970. https://doi.org/10.1038/s41598-021-85036-5

Batt, G. E., Braun, J., Kohn, B. P., & McDougall, I. (2000). Thermochronological analysis of the dynamics of the Southern Alps, New Zealand. *Geological Society of America Bulletin*, *112*(2), 250–266. https://doi.org/10.1130/0016-7606(2000)112<250:taotdo>2.0.co;2

Berger, A. L., Gulick, S. P. S., Spotila, J. A., Upton, P., Jaeger, J. M., Chapman, J. B., et al. (2008). Quaternary tectonic response to intensified glacial erosion in an orogenic wedge. *Nature Geoscience*, *1*(11), 793–799. https://doi.org/10.1038/ngeo334

Blisniuk, P. M., Stern, L. A., Chamberlain, C. P., Idleman, B., & Zeitler, P. K. (2005). Climatic and ecologic changes during Miocene surface uplift in the southern Patagonian Andes. *Earth and Planetary Science Letters*, *230*(1–2), 125–142. https://doi.org/10.1016/j.epsl.2004.11.015

Braun, J. (2002a). Quantifying the effect of recent relief changes on age–elevation relationships. *Earth and Planetary Science Letters*, *200*, 331–343. https://doi.org/10.1016/s0012-821x(02)00638-6

Braun, J. (2002b). Estimating exhumation rate and relief evolution by spectral analysis of age–elevation datasets. *Terra Nova*, *14*(3), 210–214. https://doi.org/10.1046/j.1365-3121.2002.00409.x

Braun, J. (2003). Pecube: A new finite-element code to solve the 3D heat transport equation including the effects of a time-varying, finite amplitude surface topography. *Computers & Geosciences*, *29*(6), 787–794. https://doi.org/10.1016/S0098-3004(03)00052-9

Braun, J. (2005). Quantitative constraints on the rate of landform eEvolution dDerived from low-temperature thermochronology. *Reviews in Mineralogy and Geochemistry*, *58*(1), 351–374. https://doi.org/10.2138/rmg.2005.58.13

Braun, J. (2010). The many surface expressions of mantle dynamics. *Nature Geoscience*, *3*, 825–833. https://doi.org/10.1038/ngeo1020

Braun, J., Robert, X., & Simon-Labric, T. (2013). Eroding dynamic topography. *Geophysical Research Letters*, *40*(8), 1494–1499. https://doi.org/10.1002/grl.50310

Breitsprecher, K., & Thorkelson, D. J. (2009). Neogene kinematic history of Nazca–Antarctic–Phoenix slab windows beneath Patagonia and the Antarctic Peninsula. *Tectonophysics*, *464*(1–4), 10–20. https://doi.org/10.1016/j.tecto.2008.02.013

Brocklehurst, S. H., & Whipple, K. X. (2007). Response of glacial landscapes to spatial variations in rock uplift rate. *Journal of Geophysical Research*, *112*(F2). https://doi.org/10.1029/2006JF000667

Broecker, W. S., & Denton, G. H. (1989). The role of ocean-atmosphere reorganizations in glacial cycles. *Quaternary Science Reviews*, *9*, 305–341. https://doi.org/10.1016/0277-3791(90)90026-7

Brozović, N., Burbank, D. W., & Meigs, A. J. (1997). Climatic limits on landscape development in the northwestern Himalaya. *Science*, *276*(5312), 571–574. https://doi.org/10.1126/science.276.5312.571

Cande, S. C., & Leslie, R. B. (1986). Late cenozoic tectonics of the southern Chile Trench. *Journal of Geophysical Research*, *91*(B1), 471. https://doi.org/10.1029/JB091iB01p00471

Carslaw, H. S., & Jaeger, J. C. (1959). *Conduction of heat in solids* (2nd ed.) Oxford: Clarendon Press. Retrieved from http://adsabs.harvard.edu/abs/1959chs.book.....C%E5%AF%86

Cembrano, J., Hervé, F., & Lavenu, A. (1996). The Liquiñe Ofqui fault zone: A long-lived intra-arc fault system in southern Chile. *Tectonophysics*, *259*(1–3), 55–66. https://doi.org/10.1016/0040-1951(95)00066-6

Cembrano, J., Lavenu, A., Reynolds, P., Arancibia, G., López, G., & Sanhueza, A. (2002). Late Cenozoic transpressional ductile deformation north of the Nazca–South America–Antarctica triple junction. *Tectonophysics*, *354*(3), 289–314. https://doi.org/10.1016/s0040-1951(02)00388-8

Champagnac, J.-D., Molnar, P., Sue, C., & Herman, F. (2012). Tectonics, climate, and mountain topography: Tectonics climate mountain topography. *Journal of Geophysical Research*, *117*(B2). https://doi.org/10.1029/2011JB008348

Christeleit, E. C., Brandon, M. T., & Shuster, D. L. (2017). Miocene development of alpine glacial relief in the Patagonian Andes, as revealed by low-temperature thermochronometry. *Earth and Planetary Science Letters*, *460*, 152–163. https://doi.org/10.1016/j.epsl.2016.12.019

Clague, J. J., Barendregt, R. W., Menounos, B., Roberts, N. J., Rabassa, J., Martinez, O., et al. (2020). Pliocene and early pleistocene glaciation and landscape evolution on the Patagonian Steppe, Santa Cruz province, Argentina. *Quaternary Science Reviews*, *227*, 105992. https://doi.org/10.1016/j.quascirev.2019.105992

Clapperton, C. M. (1993). Nature of environmental changes in South America at the last glacial maximum. *Palaeogeography, Palaeoclimatology, Palaeoecology*, *101*(3–4), 189–208. https://doi.org/10.1016/0031-0182(93)90012-8

Clinger, A. E., Fox, M., Balco, G., Cuffey, K., & Shuster, D. L. (2020). Detrital thermochronometry reveals that the topography along the Antarctic Peninsula is not a Pleistocene landscape. *Journal of Geophysical Research: Earth Surface*, *125*, e2019JF005447. https://doi.org/10.1029/2019JF005447

Cunningham, D. (2007). Structural and topographic characteristics of restraining bend mountain ranges of the Altai, Gobi Altai and easternmost Tien Shan. *Geological Society, London, Special Publications*, *290*(1), 219–237. https://doi.org/10.1144/SP290.7

DeMets, C., Gordon, R. G., Argus, D. F., & Stein, S. (1990). Current plate motions. *Geophysical Journal International*, *101*(2), 425–478. https://doi.org/10.1111/j.1365-246x.1990.tb06579.x

Densmore, M. S., Ehlers, T. A., & Woodsworth, G. J. (2007). Effect of Alpine glaciation on thermochronometer age-elevation profiles. *Geophysical Research Letters*, *34*(2). https://doi.org/10.1029/2006GL028371

Donelick, R. A. (2005). Apatite fission-track analysis. *Reviews in Mineralogy and Geochemistry*, *58*(1), 49–94. https://doi.org/10.2138/rmg.2005.58.3

Dunai, T. J. (2005). Forward modeling and interpretation of (U-Th)/He ages. *Reviews in Mineralogy and Geochemistry*, *58*(1), 259–274. http://dx.doi.org/10.2138/rmg.2005.58.10

Egholm, D. L., Nielsen, S. B., Pedersen, V. K., & Lesemann, J.-E. (2009). Glacial effects limiting mountain height. *Nature*, *460*(7257), 884–887. https://doi.org/10.1038/nature08263

Ehlers, T. A. (2005). Crustal thermal processes and the interpretation of thermochronometer data. *Reviews in Mineralogy and Geochemistry*, *58*(1), 315–350. https://doi.org/10.2138/rmg.2005.58.12

Ehlers, T. A., & Farley, K. A. (2003). Apatite (U-Th)/He thermochronometry: Methods and applications to problems in tectonics and surface processes. *Earth and Planetary Science Letters*, *206*, 1–14. https://doi.org/10.1016/s0012-821x(02)01069-5

Ehlers, T. A., Farley, K. A., Rusmore, M. E., & Woodsworth, G. J. (2006). Apatite (U-Th)/He signal of large-magnitude accelerated glacial erosion, southwest British Columbia. *Geology*, *34*(9), 765–768. https://doi.org/10.1130/g22507.1

Ehlers, T. A., Szameitat, A., Enkelmann, E., Yanites, B. J., & Woodsworth, G. J. (2015). Identifying spatial variations in glacial catchment erosion with detrital thermochronology. *Journal of Geophysical Research: Earth Surface*, *120*(6), 1023–1039. https://doi.org/10.1002/2014JF003432

Ehlers, T. A., Willett, S. D., Armstrong, P. A., & Chapman, D. S. (2003). Exhumation of the central Wasatch Mountains, Utah: 2. Thermokinematic model of exhumation, erosion, and thermochronometer interpretation. *Journal of Geophysical Research: Solid Earth*, *108*(B3). http://dx.doi.org/10.1029/2001jb001723

Eizenhöfer, P. R., Glotzbach, C., Büttner, L., Kley, J., & Ehlers, T. A. (2021). Turning the orogenic switch: Slab-reversal in the Eastern Alps recorded by low-temperature thermochronology. *Geophysical Research Letters*, *48*, e2020GL092121. https://doi.org/10.1029/2020GL092121

Encinas, A., Folguera, A., Riffo, R., Molina, P., Fernández Paz, L., Litvak, V. D., et al. (2019). Cenozoic basin evolution of the Central Patagonian Andes: Evidence from geochronology, stratigraphy, and geochemistry. *Geoscience Frontiers*, *10*(3), 1139–1165. https://doi.org/10.1016/j.gsf.2018.07.004

England, P., & Molnar, P. (1990). Surface uplift, uplift of rocks, and exhumation of rocks. *Geology*, *18*(12), 1173–1177. https://doi.org/10.1130/0091-7613(1990)018<1173:suuora>2.3.co;2

Farley, K. A. (2000). Helium diffusion from apatite: General behavior as illustrated by Durango fluorapatite. *Journal of Geophysical Research*, *105*(B2), 2903–2914. https://doi.org/10.1029/1999JB900348

Fattaruso, L. A., Cooke, M. L., & Dorsey, R. J. (2014). Sensitivity of uplift patterns to dip of the San Andreas fault in the Coachella Valley, California. *Geosphere*, *10*(6), 1235–1246. https://doi.org/10.1130/GES01050.1

Fick, S. E., & Hijmans, R. J. (2017). WorldClim 2: New 1-km spatial resolution climate surfaces for global land areas: New climate surfaces for global land areas. *International Journal of Climatology*, *37*(12), 4302–4315. https://doi.org/10.1002/joc.5086

Flowers, R. M., & Ehlers, T. A. (2018). Rock erodibility and the interpretation of low-temperature thermochronologic data. *Earth and Planetary Science Letters*, *482*, 312–323. https://doi.org/10.1016/j.epsl.2017.11.018 ISSN 0012-821X

Folguera, A., Encinas, A., Echaurren, A., Gianni, G., Orts, D., Valencia, V., & Carrasco, G. (2018). Constraints on the neogene growth of the central Patagonian Andes at the latitude of the Chile triple junction (45–47°S) using U/Pb geochronology in synorogenic strata. *Tectonophysics*, *744*, 134–154. https://doi.org/10.1016/j.tecto.2018.06.011

Folguera, A., & Ramos, V. A. (2011). Repeated eastward shifts of arc magmatism in the Southern Andes: A revision to the long-term pattern of Andean uplift and magmatism. *Journal of South American Earth Sciences*, *32*(4), 531–546. https://doi.org/10.1016/j.jsames.2011.04.003

Forsythe, R., & Nelson, E. (1985). Geological manifestations of ridge collision: Evidence from the Golfo de Penas-Taitao Basin, southern Chile. *Tectonics*, *4*(5), 477–495. https://doi.org/10.1029/TC004i005p00477

Fosdick, J. C., Grove, M., Hourigan, J. K., & Calderón, M. (2013). Retroarc deformation and exhumation near the end of the Andes, southern Patagonia. *Earth and Planetary Science Letters*, *361*, 504–517. https://doi.org/10.1016/j.epsl.2012.12.007

Fosdick, J. C., Romans, B. W., Fildani, A., Bernhardt, A., Calderón, M., & Graham, S. A. (2011). Kinematic evolution of the Patagonian retroarc fold-and-thrust belt and Magallanes foreland basin, Chile and Argentina, 51 30′ S. *Geological Society of America Bulletin*, *123*(9–10), 1679–1698. https://doi.org/10.1130/b30242.1

Galbraith, R. F., & Laslett, G. M. (1988). Some calculations relevant to thermal annealing of fission tracks in apatite. *Proceedings of the Royal Society of London A*, *419*, 305–321. https://doi.org/10.1098/rspa.1988.0109

Garver, J. I. (2003). Etching zircon age standards for fission-track analysis. *Radiation Measurements*, *37*(1), 47–53. https://doi.org/10.1016/S1350-4487(02)00127-0

Georgieva, V., Gallagher, K., Sobczyk, A., Sobel, E. R., Schildgen, T. F., Ehlers, T. A., & Strecker, M. R. (2019). Effects of slab-window, alkaline volcanism, and glaciation on thermochronometer cooling histories, Patagonian Andes. *Earth and Planetary Science Letters*, *511*, 164–176. https://doi.org/10.1016/j.epsl.2019.01.030

Georgieva, V., Melnick, D., Schildgen, T. F., Ehlers, T. A., Lagabrielle, Y., Enkelmann, E., & Strecker, M. R. (2016). Tectonic control on rock uplift, exhumation, and topography above an oceanic ridge collision: Southern Patagonian Andes (47°S), Chile. *Tectonics*, *35*(6), 1317–1341. https://doi.org/10.1002/2016TC004120

Glotzbach, C., Lang, K. A., Avdievitch, N. N., & Ehlers, T. A. (2019). Increasing the accuracy of (U-Th(-Sm))/He dating with 3D grain modelling. *Chemical Geology*, *506*, 113–125. https://doi.org/10.1016/j.chemgeo.2018.12.032

Glotzbach, C., van der Beek, P. A., & Spiegel, C. (2011). Episodic exhumation and relief growth in the Mont Blanc massif, Western Alps from numerical modelling of thermochronology data. *Earth and Planetary Science Letters*, *304*(3–4), 417–430. https://doi.org/10.1016/j.epsl.2011.02.020

Green, P. F., Duddy, I. R., Gleadow, A. J. W., Tingate, P. R., & Laslett, G. M. (1986). Thermal annealing of fission tracks in apatite: 1. A qualitative description. *Chemical Geology: Isotope Geoscience section*, *59*, 237–253. https://doi.org/10.1016/0168-9622(86)90074-6

Guillaume, B., Gautheron, C., Simon-Labric, T., Martinod, J., Roddaz, M., & Douville, E. (2013). Dynamic topography control on Patagonian relief evolution as inferred from low temperature thermochronology. *Earth and Planetary Science Letters*, *364*, 157–167. https://doi.org/10.1016/j.epsl.2012.12.036

Guillaume, B., Martinod, J., Husson, L., Roddaz, M., & Riquelme, R. (2009). Neogene uplift of central eastern Patagonia: Dynamic response to active spreading ridge subduction? *Tectonics*, *28*(2). https://doi.org/10.1029/2008TC002324

Guivel, C., Morata, D., Pelleter, E., Espinoza, F., Maury, R. C., Lagabrielle, Y., et al. (2006). Miocene to late quaternary Patagonian basalts (46–47°S): Geochronometric and geochemical evidence for slab tearing due to active spreading ridge subduction. *Journal of Volcanology and Geothermal Research*, *149*(3–4), 346–370. https://doi.org/10.1016/j.jvolgeores.2005.09.002

Haenel, R., Stegena, L., & Rybach, L. (1988). *Handbook of terrestrial heat-flow density determination with guidelines and recommendations of the international heat flow commission*. Springer Netherlands.

Hasterok, D., & Chapman, D. S. (2011). Heat production and geotherms for the continental lithosphere. *Earth and Planetary Science Letters*, *307*(1–2), 59–70. https://doi.org/10.1016/j.epsl.2011.04.034

Herman, F., & Brandon, M. (2015). Mid-latitude glacial erosion hotspot related to equatorial shifts in southern Westerlies. *Geology*, *43*(11), 987–990. https://doi.org/10.1130/G37008.1

Herman, F., & Braun, J. (2008). Evolution of the glacial landscape of the Southern Alps of New Zealand: Insights from a glacial erosion model. *Journal of Geophysical Research*, *113*(F2). https://doi.org/10.1029/2007JF000807

Herman, F., Copeland, P., Avouac, J. P., Bollinger, L., Maheo, G., Le Fort, P., et al. (2010). Exhumation, crustal deformation, and thermal structure of the Nepal Himalaya derived from the inversion of thermochronological and thermobarometric data and modeling of the topography. *Journal of Geophysical Research*, *115*, B06407. https://doi.org/10.1029/2008JB006126

Herman, F., Seward, D., Valla, P. G., Carter, A., Kohn, B., Willett, S. D., & Ehlers, T. A. (2013). Worldwide acceleration of mountain erosion under a cooling climate. *Nature*, *504*(7480), 423–426. https://doi.org/10.1038/nature12877

Hervé, F., Faundez, V., Calderón, M., Massonne, H.-J., & Willner, A. P. (2007b). Metamorphic and plutonic basement complexes. In T. Moreno, & W. Gibbons (Eds.), *The geology of Chile* (first, pp. 5–19). The Geological Society of London. https://doi.org/10.1144/GOCH.2

Hervé, F., Godoy, E., Parada, M. A., Ramos, V., Rapela, C., Mpodozis, C., & Davidson, J. (1987). A general view on the Chilean-Argentine Andes, with emphasis on their early history. In J. W. H. Monger, & J. Francheteau (Eds.), Geodynamics series (Vol. 18, pp. 97–113). Washington: American Geophysical Union. https://doi.org/10.1029/GD018p0097

Hervé, F., Pankhurst, R. J., Demant, A., & Ramirez, E. (1997). Age and Al-in-hornblende geobarometry in the North Patagonian batholith, Aysen, Chile. In: Géodynamique andine: Résumé étendus=Andean geodynamics: Extended abstracts. Paris: ORSTOM, 579-582. (Colloques et Séminaires). ISAG 96: Symposium International sur la Géodynamique Andine (Vol. 3). Saint-Malo (FRA) (ISBN: 2-7099-1332-1).1996/09/17-19.

Hervé, F., Pankhurst, R. J., Fanning, C. M., Calderón, M., & Yaxley, G. M. (2007a). The South Patagonian batholith: 150 my of granite magmatism on a plate margin. *Lithos*, *97*(3–4), 373–394. https://doi.org/10.1016/j.lithos.2007.01.007

Hinojosa, L. F., & Villagran, C. (1997). Historia de los bosques del sur de Sudamerica, I: Antecedentes paleobotanicos, geologicos y climaticos del Terciario del cono sur de America. *Revista Chilena de Historia Natural*, *70*, 225–239.

Hubbard, A., Hein, A. S., Kaplan, M. R., Hulton, N. R. J., & Glasser, N. (2005). A modelling reconstruction of the last glacial maximum ice sheet and its deglaciation in the vicinity of the Northern Patagonian Icefield, South America. *Geografiska Annaler: Series A, Physical Geography*, *87*(2), 375–391. https://doi.org/10.1111/j.0435-3676.2005.00264.x

Hurford, A. J. (1990). Standardization of fission track dating calibration: Recommendation by the fission track working Group of the I.U.G.S. subcommission on geochronology. *Chemical Geology*, *80*, 171–178. https://doi.org/10.1016/0168-9622(90)90025-8

Klotz, T., Pomella, H., Reiser, M., Fügenschuh, B., & Zattin, M. (2019). Differential uplift on the boundary between the Eastern and the Southern European Alps: Thermochronologic constraints from the Brenner Base Tunnel. *Terra Nova*, *31*, 281–294. https://doi.org/10.1111/ter.12398

Kufner, S. K., Schurr, B., Sippl, C., Yuan, X., Ratschbacher, L., Akbar, A. S. O. M., et al. (2016). Deep India meets deep Asia - Lithospheric indentation, delamination and break-off under Pamir and Hindu Kush (Central Asia). *Earth and Planetary Science Letters*, *435*(2016), 171–184. https://doi.org/10.1016/j.epsl.2015.11.046

Lagabrielle, Y., Scalabrino, B., Suarez, M., & Ritz, J. (2010). Mio-Piiocene glaciations of Central Patagonia: New evidence and tectonic implications. *Andean Geology*, *37*(2), 276–299. https://doi.org/10.5027/andgeoV37n2-a02

Lagabrielle, Y., Suárez, M., Malavieille, J., Morata, D., Espinoza, F., Maury, R. C., et al. (2007). Pliocene extensional tectonics in the Eastern Central Patagonian Cordillera: Geochronological constraints and new field evidence. *Terra Nova*, *19*(6), 413–424. https://doi.org/10.1111/j.1365-3121.2007.00766.x

Lagabrielle, Y., Suárez, M., Rossello, E. A., Hérail, G., Martinod, J., Régnier, M., & de la Cruz, R. (2004). Neogene to quaternary tectonic evolution of the Patagonian Andes at the latitude of the Chile triple junction. *Tectonophysics*, *385*(1–4), 211–241. https://doi.org/10.1016/j.tecto.2004.04.023

Lock, J., & Willett, S. (2008). Low-temperature thermochronometric ages in fold-and-thrust belts. *Tectonophysics*, *456*(3–4), 147–162. https://doi.org/10.1016/j.tecto.2008.03.007

McQuarrie, N., & Ehlers, T. A. (2015). Influence of thrust belt geometry and shortening rate on thermochronometer cooling ages: Insights from thermokinematic and erosion modeling of the Bhutan Himalaya: Geometry, rates, and modeled cooling ages. *Tectonics*, *34*(6), 1055–1079. https://doi.org/10.1002/2014TC003783

McQuarrie, N., & Ehlers, T. A. (2017). Techniques for understanding fold-and-thrust belt kinematics and thermal evolution. *Geological Society of America Memoir*, *213*, MWR213–02.

McQuarrie, N., Eizenhöfer, P. R., Long, S. P., Tobgay, T., Ehlers, T. A., Blythe, A. E., et al. (2019). The influence of foreland structures on hinterland cooling: Evaluating the drivers of exhumation in the eastern Bhutan Himalaya. *Tectonics*, *38*(9), 3282–3310. https://doi.org/10.1029/2018TC005340

Meesters, A. G. C. A., & Dunai, T. J. (2005). A noniterative solution of the (U-Th)/He age equation. *Geochemistry, Geophysics, Geosystems*, *6*(4). https://doi.org/10.1029/2004GC000834

Mercer, J. H., & Sutter, J. F. (1982). Late miocene-earliest Pliocene glaciation in Southern Argentina: Implications for global ice-sheet history. *Palaeogeography, Palaeoclimatology, Palaeoecology*, *38*, 185–206. https://doi.org/10.1016/0031-0182(82)90003-7

Michel, L., Ehlers, T. A., Glotzbach, C., Adams, B. A., & Stübner, K. (2018). Tectonic and glacial contributions to focused exhumation in the Olympic Mountains, Washington, USA. *Geology*, *46*(6), 491–494. https://doi.org/10.1130/G39881.1

Mitchell, S. G., & Montgomery, D. R. (2006). Influence of a glacial buzzsaw on the height and morphology of the Cascade Range in central Washington State, USA. *Quaternary Research*, *65*(01), 96–107. https://doi.org/10.1016/j.yqres.2005.08.018

Olen, S. M., Ehlers, T. A., & Densmore, M. S. (2012). Limits to reconstructing paleotopography from thermochronometer data. *Journal of Geophysical Research*, *117*(F1), F01024. https://doi.org/10.1029/2011JF001985

Pedersen, V. K., Egholm, D. L., & Nielsen, S. B. (2010). Alpine glacial topography and the rate of rock column uplift: A global perspective. *Geomorphology*, *122*(1–2), 129–139. https://doi.org/10.1016/j.geomorph.2010.06.005

Pedersen, V. K., Huismans, R. S., Herman, F., & Egholm, D. L. (2014). Controls of initial topography on temporal and spatial patterns of glacial erosion. *Geomorphology*, *223*, 96–116. https://doi.org/10.1016/j.geomorph.2014.06.028

Penck, W. (1953). *Morphological analyse of land forms*. London: MacMillan.

Pomella, H., Stipp, M., & Fügenschuh, B. (2012). Thermochronological record of thrusting and strike-slip faulting along the Giudicarie fault system (Alps, Northern Italy). *Tectonophysics*, *579*, 118–130. https://doi.org/10.1016/j.tecto.2012.04.015

Prasicek, G., Larsen, I. J., & Montgomery, D. R. (2015). Tectonic control on the persistence of glacially sculpted topography. *Nature Communications*, *6*, 8028. https://doi.org/10.1038/ncomms9028

Rak, A. J., McQuarrie, N., & Ehlers, T. A. (2017). Kinematics, exhumation, and sedimentation of the North Central Andes (Bolivia): An integrated thermochronometer and thermokinematic modeling approach. *Tectonics*, *36*(11), 2524–2554. https://doi.org/10.1002/2016TC004440

Ramos, V. (1989). Andean foothills structures in Northern Magallanes Basin, Argentina. *The American Association of Petroleum Geologicsts Builletin*, *73*(7), 887–903. https://doi.org/10.1306/44b4a28a-170a-11d7-8645000102c1865d

Ramos, V. A. (2009). Anatomy and global context of the Andes: Main geologic features and the Andean orogenic cycle. *Geological Society of America Memoir*, *204*(0), 31–65. https://doi.org/10.1130/2009.1204(0210.1130/2009.1204(02)

Ramos, V. A., & Ghiglione, M. C. (2008). Tectonic Evolution of the Patagonian Andes. In: Developments in Quaternary Sciences (Vol. 11, pp. 57–71). Elsevier. https://doi.org/10.1016/S1571-0866(07)10004-X

Reiners, P. W., Spell, T. L., Nicolescu, S., & Zanetti, K. A. (2004). Zircon (U-Th)/He thermochronometry: He diffusion and comparisons with 40Ar/39Ar dating. *Geochimica et Cosmochimica Acta*, *68*(8), 1857–1887. https://doi.org/10.1016/j.gca.2003.10.021

Reiners, P. W., Zhou, Z., Ehlers, T. A., Xu, C., Brandon, M. T., Donelick, R. A., & Nicolescu, S. (2003). Post-orogenic evolution of the Dabie Shan, Eastern China, from (U–Th)/He and fission track thermochronology. *American Journal of Science*, *303*, 489–518. https://doi.org/10.2475/ajs.303.6.489

Rivera, A., Benham, T., Casassa, G., Bamber, J., & Dowdeswell, J. A. (2007). Ice elevation and areal changes of glaciers from the Northern Patagonia Icefield, Chile. *Global and Planetary Change*, *59*(1–4), 126–137. https://doi.org/10.1016/j.gloplacha.2006.11.037

Rosenau, M., Melnick, D., & Echtler, H. (2006). Kinematic constraints on intra-arc shear and strain partitioning in southern Andes between 38°S and 42°S latitude. *Tectonics*, *25*(4). https://doi.org/10.1029/2005TC001943

Scalabrino, B., Lagabrielle, Y., Malavieille, J., Dominguez, S., Melnick, D., Espinoza, F., et al. (2010). A morphotectonic analysis of central Patagonian Cordillera: Negative inversion of the Andean belt over a buried spreading center?. *Tectonics*, *29*(2), TC2010. https://doi.org/10.1029/2009TC002453

Scalabrino, B., Ritz, J.-F., & Lagabrielle, Y. (2011). Relief inversion triggered by subduction of an active spreading ridge: Evidence from glacial morphology in Central Patagonia: Relief inversion during active spreading ridge subduction. *Terra Nova*, *23*(2), 63–69. https://doi.org/10.1111/j.1365-3121.2010.00981.x

Schildgen, T. F., van der Beek, P. A., Sinclair, H. D., & Thiede, R. C. (2018). Spatial correlation bias in late-Cenozoic erosion histories derived from thermochronology. *Nature*, *559*(7712), 89–93. https://doi.org/10.1038/s41586-018-0260-6

SERNAGEOMIN. (2003). *Mapa geológico de Chile: Versión digitalPublicación geológica digital, No. 4 (CD-ROM, versión1.0, 2003)*. Santiago: Servicio Nacional de Geología y Minería.

Shuster, D. L., Cuffey, K. M., Sanders, J. W., & Balco, G. (2011). Thermochronometry reveals headward propagation of erosion in an alpine landscape. *Science*, *332*(6025), 84–88. https://doi.org/10.1126/science.1198401

Sibbett, B. S. (1988). Size, depth and related structures of intrusions under stratovolcanoes and associated geothermal systems. *Earth-Science Reviews*, *25*(4), 291–309. https://doi.org/10.1016/0012-8252(88)90070-0

Singer, B. S., Ackert, R. P., & Guillou, H. (2004). 40Ar/39Ar and K-Ar chronology of Pleistocene glaciations in Patagonia. *GSA Bulletin*, *116*(3–4), 434–450. https://doi.org/10.1130/B25177.1

Starke, J., Ehlers, T. A., & Schaller, M. (2020). Latitudinal effect of vegetation on erosion rates identified along western South America. *Science*, *367*(6484), 1358–1361. https://doi.org/10.1126/science.aaz0840

Stock, G. M., Frankel, K. L., Ehlers, T. A., Schaller, M., Briggs, S. M., & Finkel, R. C. (2009). Spatial and temporal variations in denudation of the Wasatch Mountains, Utah, USA. *Lithosphere*, *1*(1), 34–40. https://doi.org/10.1130/L15.1

Stübner, K., Drost, K., Schoenberg, R., Böhme, M., Starke, J., & Ehlers, T. A. (2016). Asynchronous timing of extension and basin formation in the South Rhodope core complex, SW Bulgaria, and northern Greece. *Tectonics*, *35*(1), 136–159. https://doi.org/10.1002/2015TC004044

Suárez, M., De La Cruz, R., & Bell, M. C. (2007). Geología del Área Ñireguao–Baño Nuevo, Región Aisén del General Carlos Ibáñez del Campo. Servicio Nacional de Geología y Minería, Carta Geológica de Chile. *Serie Geología Básica*, *108*, 1–56.

Tesauro, M., Kaban, M. K., & Cloetingh, S. A. P. L. (2013). Global model for the lithospheric strength and effective elastic thickness. *Tectonophysics*, *602*, 78–86. https://doi.org/10.1016/j.tecto.2013.01.006

Thomson, S. N. (2002). Late Cenozoic geomorphic and tectonic evolution of the Patagonian Andes between latitudes 42°S and 46°S: An appraisal based on fission-track results from the transpressional intra-arc Liquiñe-Ofqui fault zone. *GSA Bulletin*, *114*(9), 1159–1173. https://doi.org/10.1130/0016-7606(2002)114<1159:LCGATE>2.0.CO;2

Thomson, S. N., Brandon, M. T., Tomkin, J. H., Reiners, P. W., Vásquez, C., & Wilson, N. J. (2010). Glaciation as a destructive and constructive control on mountain building. *Nature*, *467*(7313), 313–317. https://doi.org/10.1038/nature09365

Thomson, S. N., Hervé, F., & Stöckhert, B. (2001). Mesozoic-Cenozoic denudation history of the Patagonian Andes (southern Chile) and its correlation to different subduction processes. *Tectonics*, *20*(5), 693–711. https://doi.org/10.1029/2001TC900013

Tomkin, J. H. (2007). Coupling glacial erosion and tectonics at active orogens: A numerical modeling study. *Journal of Geophysical Research*, *112*(F2). https://doi.org/10.1029/2005JF000332

Tomkin, J. H., & Braun, J. (2002). The influence of alpine glaciation on the relief of tectonically active mountain belts. *American Journal of Science*, *302*(3), 169–190. https://doi.org/10.2475/ajs.302.3.169

Ton-That, T., Singer, B., Morner, N., & Rabassa, J. (1999). Datación de lavas basálticas por 40Ar/39Ar y geología glacial de la región del lago Buenos Aires, Provincia de Santa Cruz, Argentina. *Revista de La Asociación Geológica Argentina*, *54*(4), 333–352.

Touloukian, Y. S., Judd, W. R., & Roy, R. F. (1989). *Physical Properties of Rocks and Minerals. CINDAS data series on material properties, Group II, Properties of special materials, II-2*. McGraw-Hill,1981.

Turcotte, D., & Schubert, G. (2002). *Geodynamics* (p. 472). Cambridge: Cambridge University Press.

Valla, P. G., Herman, F., van der Beek, P. A., & Braun, J. (2010). Inversion of thermochronological age-elevation profiles to extract independent estimates of denudation and relief history—I: Theory and conceptual model. *Earth and Planetary Science Letters*, *295*, 511–522. https://doi.org/10.1016/j.epsl.2010.04.033

van der Meijde, M., Julià, J., & Assumpção, M. (2013). Gravity derived Moho for South America. *Tectonophysics*, *609*, 456–467. https://doi.org/10.1016/j.tecto.2013.03.023

Wakabayashi, J., Hengesh, J. V., & Sawyer, T. L. (2004). Four-dimensional transform fault processes: Progressive evolution of step-overs and bends. *Tectonophysics*, *392*(1–4), 279–301. https://doi.org/10.1016/j.tecto.2004.04.013

Wang, K., Hu, Y., Bevis, M., Kendrick, E., Smalley, R., Vargas, R. B., & Lauría, E. (2007). Crustal motion in the zone of the 1960 Chile earthquake: Detangling earthquake-cycle deformation and forearc-sliver translation: Chile earthquake crustal motion. *Geochemistry, Geophysics, Geosystems*, *8*(10), a–n. https://doi.org/10.1029/2007GC001721

Wenzens, G. (2006). Terminal Moraines, Outwash Plains, and Lake Terraces in the Vicinity of Lago Cardiel (49°S; Patagonia, Argentina)—evidence for miocene Andean foreland glaciations. *Arctic, Antarctic, and Alpine Research*, *38*(2), 276–291. https://doi.org/10.1657/1523-0430(2006)38[276:TMOPAL]2.0.CO;2

Whipp, D. M., Ehlers, T. A., Braun, J., & Spath, C. D. (2009). Effects of exhumation kinematics and topographic evolution on detrital thermochronometer data. *Journal of Geophysical Research*, *114*(F4). https://doi.org/10.1029/2008JF001195

Whipple, K. X. (2009). The influence of climate on the tectonic evolution of mountain belts. *Nature Geoscience*, *2*(2), 97–104. https://doi.org/10.1038/ngeo413

Whipple, K. X., Kirby, E., & Brocklehurst, S. H. (1999). Geomorphic limits to climate-induced increases in topographic relief. *Nature*, *401*, 39–43. https://doi.org/10.1038/43375

Whittaker, A. C. (2012). How do landscapes record tectonics and climate? *Lithosphere*, *4*(2), 160–164. https://doi.org/10.1130/RF.L003.1

Willett, C. D., Ma, K. F., Brandon, M. T., Hourigan, J. K., Christeleit, E. C., & Shuster, D. L. (2020b). Transient glacial incision in the Patagonian Andes from ~6 Ma to present. *Scientific Advances*, *12*(7), 6. https://doi.org/10.1126/sciadv.aay1641

Willett, S. D., Herman, F., Fox, M., Stalder, N., Ehlers, T. A., Jiao, R., & Yang, R. (2020a). Bias and error in modelling thermochronometric data: Resolving a potential increase in Plio-Pleistocene erosion rate. *Earth Surface Dynamics Discussion*. https://doi.org/10.5194/esurf-2020-59. [preprint]in review.

Yanites, B. J., & Ehlers, T. A. (2012). Global climate and tectonic controls on the denudation of glaciated mountains. *Earth and Planetary Science Letters*, *325–326*, 63–75. https://doi.org/10.1016/j.epsl.2012.01.030

Yanites, B. J., & Ehlers, T. A. (2016). Intermittent glacial sliding velocities explain variations in long-timescale denudation. *Earth and Planetary Science Letters*, *450*, 52–61. https://doi.org/10.1016/j.epsl.2016.06.022